Effective surface and boundary conditions for heterogeneous surfaces with mixed boundary conditions.

Jianwei Guo, Stéphanie Veran-Tissoires, Michel Quintard

http://dx.doi.org/10.1016/j.jcp.2015.10.050

Effective surface and boundary conditions for heterogeneous surfaces with mixed boundary conditions

Jianwei Guo [a], Stéphanie Veran-Tissoires [a,b,*], Michel Quintard [a,c]

[a] Université de Toulouse, INPT, UPS, IMFT (Institut de Mécanique des Fluides de Toulouse), 31400 Toulouse, France
[b] Department of Civil and Environmental Engineering, Tufts University, Medford, MA 02155, United States
[c] CNRS, IMFT, 31400 Toulouse, France

Keywords:
Heterogeneous surface
Multi-domain decomposition
Closure problems
Effective surface
Effective boundary conditions

A B S T R A C T

To deal with multi-scale problems involving transport from a heterogeneous and rough surface characterized by a mixed boundary condition, an effective surface theory is developed, which replaces the original surface by a homogeneous and smooth surface with specific boundary conditions. A typical example corresponds to a laminar flow over a soluble salt medium which contains insoluble material. To develop the concept of effective surface, a multi-domain decomposition approach is applied. In this framework, velocity and concentration at micro-scale are estimated with an asymptotic expansion of deviation terms with respect to macro-scale velocity and concentration fields. Closure problems for the deviations are obtained and used to define the effective surface position and the related boundary conditions. The evolution of some effective properties and the impact of surface geometry, Péclet, Schmidt and Damköhler numbers are investigated. Finally, comparisons are made between the numerical results obtained with the effective models and those from direct numerical simulations with the original rough surface, for two kinds of configurations.

1. Introduction

Transport phenomena taking place over heterogeneous and rough surfaces can be found in a wide range of processes, such as dissolution, drying or ablation to cite a few. The surface characteristic length-scale (linked to the heterogeneities) is generally much smaller than the scale of the global mechanism. In these circumstances, direct numerical simulations (DNSs) become difficult to achieve in practical applications. Indeed, DNSs are only possible when the two length-scales have more or less the same order of magnitude. To overcome this difficulty, a traditional way of solving such problems is to incorporate the micro-scale behaviors into a boundary condition over a smooth, "homogenized" or effective surface.

In [1–3], domain decomposition and multi-scale asymptotic analysis were first introduced to develop an effective surface and the associated boundary conditions for the flow over a rough solid–liquid surface. Later, the effective surface concept was used to describe ablation processes in aerospace [30] and nuclear safety [15] contexts. Different from these works which employed asymptotic method, Wood et al. [33] obtained a spatially smoothed jump condition for the originally non-uniform surface with volume averaging technique. For sake of simplicity, most of the previous studies ignored the geometry changes

* Corresponding author.
E-mail address: stephanie.veran@u-bordeaux.fr (S. Veran-Tissoires).

Nomenclature

Roman symbols

$\mathbf{A}$	closure variable for the velocity (dimensionless)
a	closure variable for the concentration (dimensionless)
$A_{\beta\gamma}$	surface area of the soluble material in Ω_i m^2
$A_{\beta\sigma}$	surface area of the insoluble material in Ω_i ..... m^2
$\mathbf{B}$	closure variable for the velocity ..... m
b	closure variable for the concentration ..... m
b_r	roughness width ..... m
c	concentration of the dissolved species defined in Ω ..... $\mathrm{kg\,m^{-3}}$
c_{eq}	thermodynamic equilibrium concentration of the dissolved species ..... $\mathrm{kg\,m^{-3}}$
c_i	concentration of the dissolved species defined in Ω_i ..... $\mathrm{kg\,m^{-3}}$
$\tilde{c_i}$	concentration deviation of the dissolved species in Ω_i ..... $\mathrm{kg\,m^{-3}}$
c_0	concentration of the dissolved species defined in Ω_0 ..... $\mathrm{kg\,m^{-3}}$
D	diffusion coefficient of the dissolved species ..... $\mathrm{m^2\,s^{-1}}$
Da	Damköhler number (dimensionless)
$\mathrm{Da}^v_{\mathrm{eff}}$	effective Damköhler number at Σ^v_{eff} (dimensionless)
$\widehat{\mathrm{Da}}$	mean Damköhler number over surface Σ (dimensionless)
$\mathbf{e}_1$	unit normal vector linked to x (dimensionless)
$\mathbf{e}_2$	unit normal vector linked to y (dimensionless)
h_r	roughness height ..... m
k	reaction rate coefficient at Σ ..... $\mathrm{m\,s^{-1}}$
k_γ	reaction rate coefficient at $\Sigma_{\beta\gamma}$ ..... $\mathrm{m\,s^{-1}}$
k_σ	reaction rate coefficient at $\Sigma_{\beta\sigma}$ ..... $\mathrm{m\,s^{-1}}$
k^0_{eff}	effective reaction rate coefficient at $y=0$ ..... $\mathrm{m\,s^{-1}}$
k^c_{eff}	effective reaction rate coefficient at Σ^c_{eff} ..... $\mathrm{m\,s^{-1}}$
k^v_{eff}	effective reaction rate coefficient at Σ^v_{eff} ..... $\mathrm{m\,s^{-1}}$
k^w_{eff}	effective reaction rate coefficient at $y=w$ ..... $\mathrm{m\,s^{-1}}$
$\hat{k}^v$	surface average reaction rate coefficient at Σ^v_{eff} ..... $\mathrm{m\,s^{-1}}$
l	micro-scale characteristic length ..... m
l_i	width of Ω_i ..... m
L	macro-scale characteristic length ..... m
m	closure variable for the pressure ..... $\mathrm{Pa\,s\,m^{-1}}$
$\mathbf{n}_{ls}$	unit normal vector on Σ pointing towards the solid (dimensionless)
$\mathbf{n}_{0,i}$	unit normal vector on $\Sigma_{0,i}$ pointing towards the wall (dimensionless)
p	pressure defined in Ω ..... Pa
p_0	pressure defined in Ω_0 ..... Pa
p_i	pressure defined in Ω_i ..... Pa
Pe_l	micro-scale Péclet number (dimensionless)
$\tilde{p}_i$	pressure deviation defined in Ω_i ..... Pa
Re_l	micro-scale Reynolds number (dimensionless)
Re_L	macro-scale Reynolds number (dimensionless)
s	closure variable for the pressure ..... Pa s
Sc	micro-scale Schmidt number (dimensionless)
$\mathbf{u}$	fluid velocity defined in Ω ..... $\mathrm{m\,s^{-1}}$
$\mathbf{u}_i$	fluid velocity defined in Ω_i ..... $\mathrm{m\,s^{-1}}$
$\tilde{\mathbf{u}}_i$	fluid velocity deviation in Ω_i ..... $\mathrm{m\,s^{-1}}$
$\mathbf{u}_0$	fluid velocity defined in Ω_0 ..... $\mathrm{m\,s^{-1}}$
U	magnitude of macro-scale velocity ..... $\mathrm{m\,s^{-1}}$
w^c_x	distance between Σ_0 and Σ^c_{eff} ..... m
w^v_x	distance between Σ_0 and Σ^v_{eff} ..... m
x	abscissa ..... m
y	ordinate ..... m

Greek symbols

β	subscript referring to the fluid phase
δ	effective surface position ..... m
δ_c	position of effective surface under thermodynamic equilibrium (dimensionless)
δ_v	position of effective surface with no-slip condition (dimensionless)
γ	subscript referring to soluble phase
σ	subscript referring to insoluble phase
μ	fluid dynamic viscosity ..... Pa s
Ω	global domain
Ω_0	subdomain associated with length scale L
Ω_i	pseudo-periodic unit cell
ρ	fluid density ..... $\mathrm{kg\,m^{-3}}$
ρ_γ	density of soluble medium ..... $\mathrm{kg\,m^{-3}}$
ρ_σ	density of insoluble material ..... $\mathrm{kg\,m^{-3}}$
Σ	rough solid–liquid interface
$\Sigma_{\beta\gamma}$	interface between β and γ phases
$\Sigma_{\beta\sigma}$	interface between β and σ phases
Σ_0	fictitious surface separating Ω_0 and Ω_i
$\Sigma_{0,i}$	restriction of Σ_0 in Ω_i
Σ_e	upper surface of Ω
Σ^c_{eff}	effective surface under thermodynamic equilibrium
Σ^v_{eff}	effective surface with no-slip boundary condition
Σ_l	lateral surface of Ω
$\Sigma_{l,i}$	periodic surface lateral surface of Ω_i

and considered fixed boundaries. In a few studies, these geometry changes were taken into consideration. Vignoles et al. [31] ran DNSs for ablation of heterogeneous media. A recent study by Kumar et al. [21] also considered geometry changes explicitly when upscaling the reactive flow in a domain with oscillating boundaries, using matched asymptotic expansions.

While there are some similarities, one should not mix the solid–liquid problem with the problem of fluid flowing over a porous medium domain. For this latter case, one seeks to link a macro-scale description of the flow in the porous medium (e.g. Darcy's law) to a free fluid flow description in the channel (e.g., Navier–Stokes or Stokes equations). Different effective boundary conditions have been proposed [6,10,26] for the momentum balance equations. Formal developments using homogenization techniques can be found in [10,17,18,20,26]. Different upscaling methods such as volume averaging and asymptotic expansions have been implemented in order to obtain effective boundary conditions for various transport problems [1,9,13,24,25,29,32].

In this work, the problem under consideration is mass and momentum transfer in a laminar boundary layer over a heterogeneous rough surface with mixed boundary conditions. Part of the surface is subject to a Dirichlet condition or a reactive Neumann condition while the rest is subject to a no-flux Neumann condition. Such problems arise, for instance, when dealing with dissolution processes, especially on large-scale cavity formation in geological structures (solution mining, karst formations, etc.). The geometry, propagation and some other aspects related to roughnesses generated by dissolution were studied experimentally and theoretically in [7]. A similar mathematical problem appears when one considers the drying rate of a porous surface with wet and dry patches [27] or for atmosphere-scale problems [5]. Taking the development of karstic cavity for example, it often involves multi-scale problems as schematically represented in Fig. 1. It is generally difficult to take into consideration the small-scale heterogeneities over the wall surface while working at the cavity scale. Therefore, the implemented models of such dissolution problems take in practice the form of an effective surface modeling, with a heuristic boundary condition. In general one uses the Dirichlet condition as the macro-scale boundary condition, even if heterogeneities (e.g., insoluble material) and roughnesses are present. The position of the effective surface itself is guided by meshing consideration without an explicit link to the physics of the problem. These questions are addressed in this paper and a methodology is proposed to build and position the effective surface with appropriate boundary conditions.

Two length scales are important to describe the phenomena taking place at the rough surface: one is the characteristic length of the large-scale cavity, L, for instance the depth of the large-scale boundary layer developing over the rough surface, and the other one is the roughness length scale l. As illustrated in Fig. 1, a fluid β in domain Ω is flowing over a rough, heterogeneous surface Σ, made of a salt medium γ and an insoluble material σ. Mass transport over the rough surface in contact with the fluid can be modeled by different boundary conditions. In case I, the surface is assumed to be composed by patches under thermodynamic equilibrium ($\Sigma_{\beta\gamma}$), with surrounding areas with no flux ($\Sigma_{\beta\sigma}$). In case II, the boundary condition at $\Sigma_{\beta\gamma}$ is replaced by a reactive one. Generally, the surface dissolution rate of a chemical species can be expressed under the form [16,22]:

$$R_{diss} = k_s \left(1 - \frac{c_s}{c_{eq}}\right)^n \tag{1}$$

where c_s is the total chemical concentration at the surface, c_{eq} the equilibrium concentration with respect to the dissolving species and k_s the surface reaction rate coefficient.

The steady-state mass and momentum transfer problem can be described as follows

Pb I in Ω

$$\rho\,(\mathbf{u}\cdot\nabla)\,\mathbf{u} - \mu\triangle\mathbf{u} + \nabla p = 0 \qquad \text{in } \Omega \tag{2}$$

$$\nabla\cdot\mathbf{u} = 0 \qquad \text{in } \Omega \tag{3}$$

$$\mathbf{u}\cdot\nabla c = \nabla\cdot(D\nabla c) \qquad \text{in } \Omega \tag{4}$$

$$\mathbf{u} = 0 \qquad \text{at } \Sigma \tag{5}$$

$$\text{(B.C. I)} \quad c = c_{eq} \qquad \text{at } \Sigma_{\beta\gamma} \tag{6}$$

$$\text{or (B.C. II)} \quad -\mathbf{n}_{ls}\cdot D\nabla c = -k_\gamma\, c_{eq}\left(1 - \tfrac{c}{c_{eq}}\right) \qquad \text{at } \Sigma_{\beta\gamma} \tag{7}$$

$$-\mathbf{n}\cdot D\nabla c = 0 \qquad \text{at } \Sigma_e,\ \Sigma_{\beta\sigma} \text{ and } \Sigma_r \tag{8}$$

$$c = 0 \qquad \text{at } \Sigma_l \tag{9}$$

$$\mathbf{n}\cdot(-p\mathbf{I} + \mu(\nabla\mathbf{u} + \nabla\mathbf{u}^T)) = \mathbf{0} \qquad \text{at } \Sigma_e \text{ and } \Sigma_r \tag{10}$$

$$\mathbf{u} = U_0\mathbf{e}_1 \qquad \text{at } \Sigma_l \tag{11}$$

where, k_γ is the reaction rate coefficient in $\mathrm{m\,s^{-1}}$, $\mathbf{n}$ is the normal vector pointing outward from the studied domain at Σ_e, Σ_l, Σ_r and the later mentioned $\Sigma_{l,i}$, and U_0 denotes the magnitude of the inlet velocity. One has $\mathbf{n} = \mathbf{n}_{ls}$ at $\Sigma_{\beta\sigma}$, with $\mathbf{n}_{ls}$ the normal vector of Σ pointing towards the solid phase. B.C. I and B.C. II refer to case I and case II problems, respectively. It is worthy noticing that the no flux condition at Σ_e and the constant velocity condition at Σ_l are not unique, which can be replaced, for instance, by zero concentration condition at Σ_e and constant pressure at Σ_l, respectively.

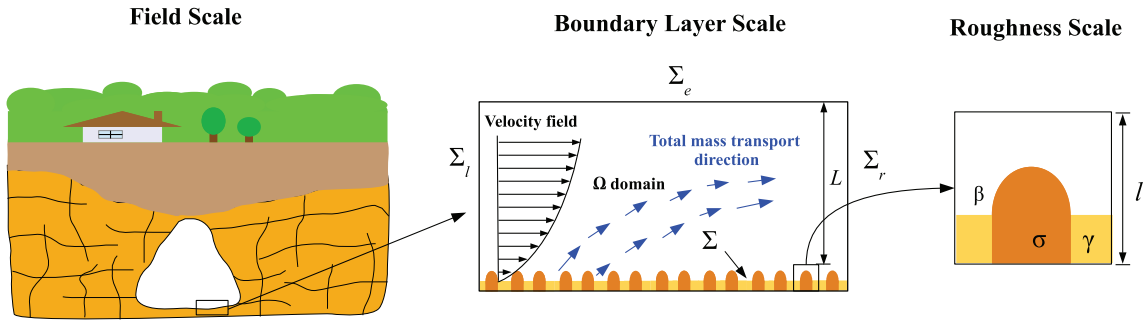

Fig. 1. Multi-scale description of the system. The dissolving medium is denoted as γ-phase and the non-dissolving part as σ-phase.

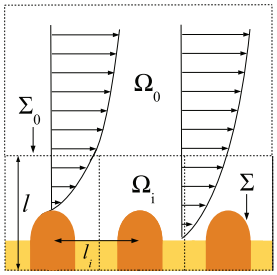

Fig. 2. Close-up view of the velocity field near the rough surface.

Eq. (7) has a form similar to the rate laws proposed in [11,12,28] for limestone and gypsum dissolution. First order reaction, i.e., $n = 1$, is considered in this study. Additional assumptions are used: the fluid is incompressible and its physical properties do not vary significantly with concentration. Hydrostatic pressure has been included in the field p. While we have in mind potential evolution of the surface Σ due to the dissolution process, it was assumed that the relaxation time for the transport problem is smaller at the roughness scale than the one of the dissolution process. Therefore, the transport problem is considered at steady-state for a given geometry. Such an assumption is valid when the momentum balance problem is independent of the concentration field, i.e., the velocity of geometry evolution is small compared to the relaxation of the viscous flow. For instance in the case of gypsum dissolution in water, the characteristic times for the viscous flow relaxation and the interface dissolution are about 1 s and 10^4 s, respectively, for a characteristic length of 1 mm. This example is representative of our considered condition. The evolution of the geometry is not within the scope of this paper.

A typical solution of this multi-scale problem would feature large-scale evolution of the pressure, velocity and concentration far from the surface and deviations from this large-scale pattern in the neighborhood of the roughnesses. This situation is schematically represented in Fig. 2. A bulk domain Ω_0 is defined where the variables do not show fluctuations induced by the roughnesses at the l-scale, and a series of elementary volumes Ω_i are defined which contain the wall perturbations, roughness and heterogeneity. Assuming periodicity is typical of most situations and this assumption is adopted in this paper. Clearly, this suggests that some kind of effective boundary condition may be imposed at the surface of Σ_0 in order to reproduce the same bulk fields. One technique to derive effective surface and effective boundary conditions is based on a multi-domain decomposition method, as illustrated by [1,15,30]. The idea is to solve the flow and mass transport problems in each Ω_i by introducing an asymptotic expansion of deviation terms based on the macro-scale bulk velocity and concentration fields. In general, closure problems may be found for variables mapping the deviations onto the bulk variables and their derivatives. This can be used to provide a set of effective boundary conditions applied at the boundary Σ_0. It is often interesting to place the effective surface in a location different from Σ_0 for sake of efficiency, which will be discussed in Section 3. Effective parameter calculations will be provided in Section 4. Finally, two comparisons of direct numerical simulations results and effective surface results are given in Section 5, which allows us to discuss the practical implementation of the effective surface model, and in particular the choice of the "optimal" position of the effective surface.

2. Multi-domain decomposition

As previously introduced, the characteristic length-scale of the rough heterogeneous surface, l, is much smaller than the one of the global domain Ω, L, e.g., the depth of the large-scale boundary layer. Therefore, we can assume that all fluctuations of velocity and concentration resulting from the wall non-uniformity vanish far from the wall. The Ω domain may be decomposed into a global external subdomain Ω_0 (with $\star_0$ quantities) and local subdomains Ω_i (with $\star_i$ quantities) by introducing an arbitrary surface Σ_0, as done in [1,15,30]. Surface Σ_0 should be located at an appropriate position to ensure that all fluctuations are contained in Ω_i subdomains and that the assumption $l \ll L$ is valid. This decomposition is illustrated in Fig. 3.

With the assumption that the wall surface Σ has a periodic structure, the initial problem can be decomposed into a Ω_0 problem and a series of Ω_i problems. For sake of simplicity, the development is presented in 2D ($(\mathbf{e}_1, \mathbf{e}_2)$ plane) and

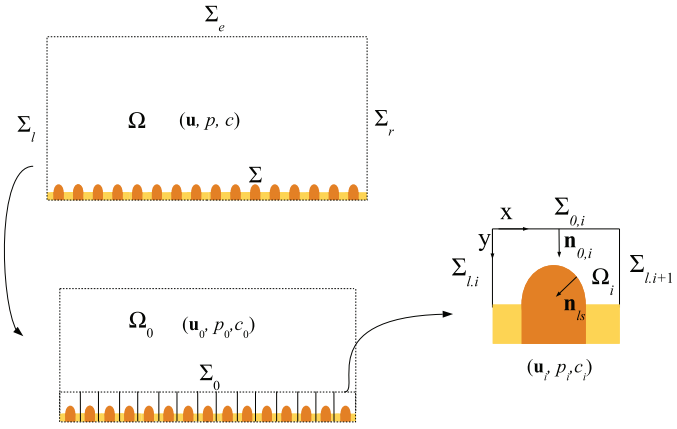

Fig. 3. Multi-domain decomposition.

is sketched in Fig. 3. Vector $\mathbf{e}_1$ (x-coordinate) corresponds to the infinite flow direction, $\mathbf{e}_2$ (y-coordinate) and $\mathbf{n}_{0,i}$, the normal vector to $\Sigma_{0,i}$, are pointing from Ω_0 towards Ω_i. Velocity, pressure, concentration, mass flux and stress tensor are continuous across the fictitious surface $\Sigma_{0,i}$, which refers to the intersection between Ω_0 and Ω_i:

$$\mathbf{u}_0 = \mathbf{u}_i \tag{12}$$

$$p_0 = p_i \tag{13}$$

$$c_0 = c_i \tag{14}$$

$$\mathbf{n}_{0,i} \cdot (-D\nabla c_0 + \mathbf{u}_0 c_0) = \mathbf{n}_{0,i} \cdot (-D\nabla c_i + \mathbf{u}_i c_i) \tag{15}$$

$$\mathbf{n}_{0,i} \cdot (-p_0\mathbf{I} + \mu(\nabla\mathbf{u}_0 + \nabla\mathbf{u}_0^T)) = \mathbf{n}_{0,i} \cdot (-p_i\mathbf{I} + \mu(\nabla\mathbf{u}_i + \nabla\mathbf{u}_i^T)) \tag{16}$$

With these continuity conditions taken into account, the decomposed Ω_0 and Ω_i problems can be written separately as follows:

Pb II (in Ω_0) (i.e., macro-scale problem)

$$\rho\,(\mathbf{u}_0 \cdot \nabla)\,\mathbf{u}_0 - \mu\triangle\mathbf{u}_0 + \nabla p_0 = 0 \quad \text{in } \Omega_0 \tag{17}$$

$$\nabla \cdot \mathbf{u}_0 = 0 \quad \text{in } \Omega_0 \tag{18}$$

$$\mathbf{u}_0 \cdot \nabla c_0 = \nabla \cdot (D\nabla c_0) \quad \text{in } \Omega_0 \tag{19}$$

$$c_0 = 0 \quad \text{at } \Sigma_l/\Omega_0 \tag{20}$$

$$-\mathbf{n} \cdot D\nabla c_0 = 0 \quad \text{at } \Sigma_e \text{ and } \Sigma_r/\Omega_0 \tag{21}$$

$$\mathbf{n} \cdot (-p_0\mathbf{I} + \mu(\nabla\mathbf{u}_0 + \nabla\mathbf{u}_0^T)) = \mathbf{0} \quad \text{at } \Sigma_e \text{ and } \Sigma_r/\Omega_0 \tag{22}$$

$$\mathbf{u}_0 = U_0\mathbf{e}_1 \quad \text{at } \Sigma_l/\Omega_0 \tag{23}$$

where, Σ_l/Ω_0 and Σ_r/Ω_0 denote the parts of lateral boundaries contained in Ω_0.

Pb III (in Ω_i) (i.e., micro-scale problem)

$$\rho\,(\mathbf{u}_i \cdot \nabla)\,\mathbf{u}_i - \mu\triangle\mathbf{u}_i + \nabla p_i = 0 \quad \text{in } \Omega_i \tag{24}$$

$$\nabla \cdot \mathbf{u}_i = 0 \quad \text{in } \Omega_i \tag{25}$$

$$\mathbf{u}_i \cdot \nabla c_i = \nabla \cdot (D\nabla c_i) \quad \text{in } \Omega_i \tag{26}$$

$$\mathbf{u}_i\,(x + l_i) = \mathbf{u}_i(x) \quad \text{at } \Sigma_{l,i} \tag{27}$$

$$p_i\,(x + l_i) = p_i(x) \quad \text{at } \Sigma_{l,i} \tag{28}$$

$$\mathbf{n} \cdot (-p_i\mathbf{I} + \mu(\nabla\mathbf{u}_i + \nabla\mathbf{u}_i^T)) = \mathbf{0} \quad \text{at } \Sigma_{l,i} \text{ and } \Sigma_{0,i} \tag{29}$$

$$c_i\,(x + l_i) = c_i(x) \quad \text{at } \Sigma_{l,i} \tag{30}$$

$$\mathbf{u}_i = 0 \quad \text{at } \Sigma \tag{31}$$

$$-\mathbf{n} \cdot D\nabla c_i = 0 \quad \text{at } \Sigma_{\beta\sigma} \text{ and } \Sigma_{l,i} \tag{32}$$

$$\text{(B.C. I)} \qquad c_i = c_{eq} \quad \text{at } \Sigma_{\beta\gamma} \tag{33}$$

$$\text{or (B.C. II)} \qquad -\mathbf{n}_{ls} \cdot D\nabla c_i = -k_\gamma\, c_{eq}\left(1 - \tfrac{c_i}{c_{eq}}\right) \quad \text{at } \Sigma_{\beta\gamma} \tag{34}$$

The periodic boundary conditions are based on the assumption that the transverse flux through $\Sigma_{l,i}$ is negligible compared to the one across $\Sigma_{0,i}$.

Solving these problems in a direct manner will make little benefit compared to DNSs. To gain computational efficiency, one should seek for generic expressions of variables in Ω_i subdomains and describe the microscopic behaviors by some kind of averaging, instead of considering all the details induced by the surface non-uniformity. Asymptotic expansions are used in the next section to estimate $\mathbf{u}_i$ and c_i at first order. By solving the closure problems, these estimates are found and effective boundary conditions are built for effective surfaces defined at different positions.

3. Effective boundary conditions

Since first proposed by Carrau [8], effective boundary conditions, or wall laws, have been the research topic of many scholars. With a multi-domain decomposition technique and an asymptotic approach, Achdou et al. [1–4] studied both mathematically and numerically the problem of laminar flows over periodic rough surfaces with no-slip condition. This problem was reviewed by Jäger and Mikelić, including the problem of the interface between a liquid domain and a porous domain [18–20]. Veran et al. [30] and Introïni et al. [15] developed the concept of effective surface for momentum and mass (or heat) transfer on a rough surface, with a particular attention on the question of positioning the effective surface. This paper makes use of similar ideas, incorporating not only the reactive case as in [30] (with a different expression of the reaction rate suitable for dissolution problems), but also the case of surface under thermodynamic equilibrium and taking into account parts of the surface corresponding to insoluble or non-reactive material.

In this section, the momentum and mass transfer problems are solved separately. Assuming that the flow properties are independent of c, the momentum problem can be decoupled from the mass transport one. The momentum transfer problem has already been worked out in the above cited literature. Therefore, the development is reviewed rapidly for the reader's understanding, following notations and presentation proposed in [15,30]. First, estimates of $\mathbf{u}_i$ and p_i are made by the sum of macroscopic terms and deviations. Then the macroscopic terms are developed by Taylor expansion from Σ_0. The deviation terms are decomposed by means of closure mapping variables. Closure problems are then used to get first order estimates of the deviations, and this in turn can be used to determine the effective boundary conditions. The problem for mass transfer is solved in a similar manner.

3.1. Momentum effective boundary conditions

As detailed previously, the micro-scale variables are partitioned as shown below

$$\mathbf{u}_i = \mathbf{u} + \tilde{\mathbf{u}}_i, \qquad p_i = p + \tilde{p}_i \tag{35}$$

where, $\tilde{\mathbf{u}}_i$, $\tilde{p}_i$ and later mentioned $\tilde{c}_i$ are the deviations, defined as the difference between micro- and macro-scale variables. The global field $\mathbf{u}$ and p are equal to $\mathbf{u}_0$ and p_0 in Ω_0 and are smooth continuations of these fields in Ω_i. Approximating $\mathbf{u}$ and p in Ω_i with Taylor expansion in the normal direction to Σ_0, $\mathbf{u}_i$ and p_i can be estimated as

$$\mathbf{u}_i = \mathbf{u}_0|_{y=0} + \mathbf{y}\cdot\nabla\mathbf{u}_0|_{y=0} + \frac{1}{2}\mathbf{y}\mathbf{y}\cdot\nabla\nabla\mathbf{u}_0|_{y=0} + \cdots + \tilde{\mathbf{u}}_i \tag{36}$$

$$p_i = p_0|_{y=0} + \mathbf{y}\cdot\nabla p_0|_{y=0} + \frac{1}{2}\mathbf{y}\mathbf{y}\cdot\nabla\nabla p_0|_{y=0} + \cdots + \tilde{p}_i \tag{37}$$

First order estimates of $\mathbf{u}_i$ and p_i are

$$\mathbf{u}_i = \mathbf{u}_0|_{y=0} + \mathbf{y}\cdot\nabla\mathbf{u}_0|_{y=0} + \tilde{\mathbf{u}}_i, \qquad p_i = p_0|_{y=0} + \mathbf{y}\cdot\nabla p_0|_{y=0} + \tilde{p}_i \tag{38}$$

In a developed boundary layer, the velocity is mainly tangential and the gradients for both velocity and pressure are dominated by the components normal to the wall, i.e., $\frac{\partial}{\partial x} \ll \frac{\partial}{\partial y}$. Therefore, the first order term of the above estimates can be rewritten as

$$\mathbf{y}\cdot\nabla\mathbf{u}_0|_{y=0} = y\frac{\partial u_0}{\partial y}\Big|_{y=0}\mathbf{e}_1, \qquad \mathbf{y}\cdot\nabla p_0|_{y=0} = y\frac{\partial p_0}{\partial y}\Big|_{y=0} \tag{39}$$

Taking into consideration the no-slip boundary condition described by Eq. (31), the following relation between the different velocities may be written in terms of order of magnitude

$$O\left(\tilde{\mathbf{u}}_i\right) = O\left(\mathbf{u}_0|_{y=0}\right) = O\left(\frac{l}{L}U\right) \tag{40}$$

with U denoting the magnitude of the global velocity $\mathbf{u}$ and L the depth of the bulk flow boundary layer.

In order to characterize the flow features at the different length-scales, the macro- and micro-scale Reynolds numbers are defined as $\mathrm{Re}_L = \frac{\rho UL}{\mu}$ and $\mathrm{Re}_l = \frac{\rho \epsilon Ul}{\mu}$, respectively, where $\epsilon = \frac{l}{L}$ and the reference velocity in the roughness domain is

estimated linearly as compared to U. From these two definitions, one can write immediately

$$\mathrm{Re}_l = \epsilon^2 \mathrm{Re}_L \tag{41}$$

Assuming the flow is laminar implies that the boundary layer thickness scales as $\mathrm{Re}_L^{-\frac{1}{2}}$. Taking into consideration also that $\epsilon \ll 1$ due to the assumption of $l \ll L$, one obtains $\mathrm{Re}_L \ll \epsilon^{-2}$. By substituting this relation into Eq. (41), it gives $\mathrm{Re}_l \ll 1$.

Substituting the approximations of $\mathbf{u}_i$ and p_i defined by Eq. (35) into Eq. (24) and then subtracting Eq. (2) give

$$\rho\left(\mathbf{u}\cdot\nabla\right)\tilde{\mathbf{u}}_i + \rho\left(\tilde{\mathbf{u}}_i\cdot\nabla\right)\mathbf{u} + \rho\left(\tilde{\mathbf{u}}_i\cdot\nabla\right)\tilde{\mathbf{u}}_i - \mu\triangle\tilde{\mathbf{u}}_i + \nabla\tilde{p}_i = 0 \text{ in } \Omega_i \tag{42}$$

which can be expressed in a dimensionless form as

$$\mathrm{Re}_l\left(\mathbf{u}'\cdot\nabla'\right)\tilde{\mathbf{u}}_i' + \mathrm{Re}_l\left(\tilde{\mathbf{u}}_i'\cdot\nabla'\right)\mathbf{u}' + \mathrm{Re}_l\left(\tilde{\mathbf{u}}_i'\cdot\nabla'\right)\tilde{\mathbf{u}}_i' - \triangle'\tilde{\mathbf{u}}_i' + \nabla'\tilde{p}_i{}' = 0 \text{ in } \Omega_i \tag{43}$$

with the dimensionless variables ($\star'$ quantities) defined as

$$\mathbf{u}' = \frac{\mathbf{u}}{\epsilon U}\ , \quad \nabla' = l\nabla, \quad \tilde{\mathbf{u}}_i' = \frac{\tilde{\mathbf{u}}_i}{\epsilon U}\ , \quad \tilde{p}_i{}' = \frac{\tilde{p}_i l}{\mu\epsilon U} \tag{44}$$

Given that $\mathrm{Re}_l \ll 1$, Eq. (43) can be simplified by omitting the first three terms. Going back to the dimensional form, we have

$$-\mu\triangle\tilde{\mathbf{u}}_i + \nabla\tilde{p}_i = 0 \tag{45}$$

Hereby the Navier–Stokes equations have been transformed into a Stokes problem in Ω_i, similarly to that proposed in [15,18,30].

The other equations of the boundary value problem can be obtained by analogy to Eq. (42), and they can be summarized as

Pb $\mathrm{III}_{\tilde{\mathbf{u}}_i}$ (in Ω_i):

$$-\mu\triangle\tilde{\mathbf{u}}_i + \nabla\tilde{p}_i = 0 \qquad \text{in } \Omega_i \tag{46}$$

$$\nabla\cdot\tilde{\mathbf{u}}_i = 0 \qquad \text{in } \Omega_i \tag{47}$$

$$\mathbf{n}\cdot(-\tilde{p}_i\mathbf{I} + \mu(\nabla\tilde{\mathbf{u}}_i + \nabla\tilde{\mathbf{u}}_i^T)) = \mathbf{0} \qquad \text{at } \Sigma_{0,i} \text{ and } \Sigma_{l,i} \tag{48}$$

$$\tilde{p}_i = 0 \qquad \text{at } \Sigma_{0,i} \tag{49}$$

$$\tilde{\mathbf{u}}_i(x + l_i) = \tilde{\mathbf{u}}_i(x) \qquad \text{at } \Sigma_{l,i} \tag{50}$$

$$\tilde{p}_i(x + l_i) = \tilde{p}_i(x) \qquad \text{at } \Sigma_{l,i} \tag{51}$$

$$u_0|_{y=0}\mathbf{e}_1 + y\frac{\partial u_0}{\partial y}\Big|_{y=0}\mathbf{e}_1 + \tilde{\mathbf{u}}_i = 0 \qquad \text{at } \Sigma \tag{52}$$

So far, the resolution of this set of equations still remains expensive, due to the coupling of micro- and macro-scale variables. As discussed in [15], and given the linear structure of the problem, the macroscopic terms can be considered to be generators of the deviations. From Eq. (52), it is obvious that if the terms with macroscopic variables are zero, the deviations of velocity and pressure will both go zero. Therefore, the deviation terms can be represented in the following form:

$$(1)\quad \tilde{\mathbf{u}}_i = \mathbf{A}u_0|_{y=0} + \mathbf{B}\frac{\partial u_0}{\partial y}\Big|_{y=0}, \qquad (2)\quad \tilde{p}_i = mu_0|_{y=0} + s\frac{\partial u_0}{\partial y}\Big|_{y=0} \tag{53}$$

Closure problems for closure variables $(\mathbf{A}, m)$ and $(\mathbf{B}, s)$ are given by Pb $\mathrm{III}_{(\mathbf{A},m)}$ and Pb $\mathrm{III}_{(\mathbf{B},s)}$ as presented in Appendix B, obtained by substituting Eq. (53) into Pb $\mathrm{III}_{\tilde{\mathbf{u}}_i}$ and collecting terms involving $u_0|_{y=0}$ and $\frac{\partial u_0}{\partial y}\big|_{y=0}$, respectively. At this point, one can see that $(\mathbf{A}, m) = (-\mathbf{e}_1, 0)$ is a solution for closure problem Pb $\mathrm{III}_{(\mathbf{A},m)}$. Inserting this solution into Eq. (53)(1) gives

$$\tilde{\mathbf{u}}_i = -u_0|_{y=0}\mathbf{e}_1 + \mathbf{B}\frac{\partial u_0}{\partial y}\Big|_{y=0} \tag{54}$$

According to velocity continuity at $\Sigma_{0,i}$, we have $\tilde{\mathbf{u}}_i|_{y=0} = 0$. By introducing $w_x^v = -B|_{y=0}$, with B the x-component of $\mathbf{B}$, the velocity at $\Sigma_{0,i}$ can be written as

$$\mathbf{u}_0|_{y=0} = u_0|_{y=0}\mathbf{e}_1 = -w_x^v\frac{\partial u_0}{\partial y}\Big|_{y=0}\mathbf{e}_1 \quad \text{at } \Sigma_{0,i} \tag{55}$$

which has the form of a Navier condition.

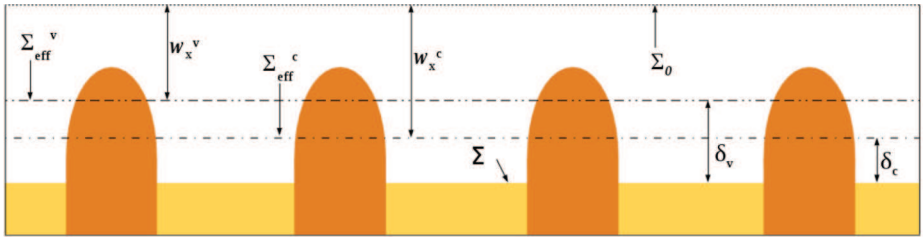

Fig. 4. Schematic illustration of the position of the different effective surfaces, where δ_v and δ_c are not normalized with respect to h_r.

Following [15,30], it is interesting to look at the modification of this boundary condition for another position of the effective surface. For a given effective surface Σ_{eff} defined at position $y = w$, a first order Taylor expansion allows us to write

$$\mathbf{u}_0|_{y=w} = \mathbf{u}_0|_{y=0} + w\frac{\partial u_0}{\partial y}\Big|_{y=0}\mathbf{e}_1 \tag{56}$$

which can be rewritten as

$$\mathbf{u}_0|_{y=w} = \left(w - w_x^v\right)\frac{\partial u_0}{\partial y}\Big|_{y=0}\mathbf{e}_1 \text{ at } \Sigma_{\text{eff}} \tag{57}$$

by substituting Eq. (55).

Up to this point, the homogenization procedure enables to build the effective momentum boundary conditions, which depend on the choice of the effective surface position. It is seen that at the position defined by $y = w_x^v$ one can recover a no-slip boundary condition (cf. Fig. 4), which plays an important role in the macro-scale simulations as shown later.

3.2. Mass effective boundary condition

In this section, the same homogenization method is applied to the mass transfer problem. First order estimate for c_i can be written as

$$c_i = c_0|_{y=0} + y\frac{\partial c_0}{\partial y}\Big|_{y=0} + \tilde{c}_i \tag{58}$$

Consequently, Eq. (26) can be transformed into

$$v\frac{\partial c_0}{\partial y}\Big|_{y=0} + \mathbf{u}_i \cdot \nabla\tilde{c}_i = \nabla \cdot \left(D\nabla\tilde{c}_i\right) \tag{59}$$

with $v = \mathbf{u}_i \cdot \mathbf{e}_2$. The mass boundary conditions can be rewritten as

$$-\mathbf{n} \cdot \left(D\frac{\partial c_0}{\partial y}\Big|_{y=0}\mathbf{e}_2\right) - \mathbf{n} \cdot D\nabla\tilde{c}_i = 0 \qquad \text{at } \Sigma_{\beta\sigma} \text{ and } \Sigma_{l.i} \tag{60}$$

$$\tilde{c}_i\,(x + l_i) = \tilde{c}_i(x) \qquad \text{at } \Sigma_{l,i} \tag{61}$$

$$\tilde{c}_i = 0 \qquad \text{at } \Sigma_{0,i} \tag{62}$$

$$\text{(B.C. I)} \quad c_0|_{y=0} + y\frac{\partial c_0}{\partial y}\Big|_{y=0} + \tilde{c}_i = c_{eq} \qquad \text{at } \Sigma_{\beta\gamma} \tag{63}$$

$$\text{or (B.C. II)} \quad -\mathbf{n}_{ls} \cdot \left(D\frac{\partial c_0}{\partial y}\Big|_{y=0}\mathbf{e}_2\right) - \mathbf{n}_{ls} \cdot D\nabla\tilde{c}_i = -k_\gamma\, c_{eq}\left(1 - \frac{c_0|_{y=0} + y\frac{\partial c_0}{\partial y}|_{y=0} + \tilde{c}_i}{c_{eq}}\right) \text{ at } \Sigma_{\beta\gamma} \tag{64}$$

which must be completed with the momentum equations, such as the Navier–Stokes equation illustrated by Eq. (24) and the corresponding boundary conditions illustrated by Eqs. (29) and (31). To solve this problem, a solution for $\tilde{c}_i$ should be sought by linking the deviation to the macroscopic concentration, which writes

$$\tilde{c}_i = a(c_0|_{y=0} - c_{eq}) + b\frac{\partial c_0}{\partial y}\Big|_{y=0} \tag{65}$$

where a and b are first-order mapping variables.

Substituting Eq. (65) into Eqs. (60), (63) and (64), we get

$$-\mathbf{n} \cdot \left(D\frac{\partial c_0}{\partial y}\Big|_{y=0}(\mathbf{e}_2 + \nabla b)\right) - \mathbf{n} \cdot D\left(c_0|_{y=0} - c_{eq}\right)\nabla a = 0 \text{ at } \Sigma_{\beta\sigma} \text{ and } \Sigma_{l.i} \tag{66}$$

$$\text{(B.C. I)} \quad (1 + a)(c_0|_{y=0} - c_{eq}) + (y + b)\frac{\partial c_0}{\partial y}\Big|_{y=0} = 0 \quad \text{at } \Sigma_{\beta\gamma} \tag{67}$$

$$\text{or (B.C.II)} \quad -\mathbf{n}_{ls}\cdot\left(D\frac{\partial c_0}{\partial y}\Big|_{y=0}(\mathbf{e}_2+\nabla b)\right)-\mathbf{n}_{ls}\cdot D\left(c_0|_{y=0}-c_{eq}\right)\nabla a$$
$$= k_\gamma\, c_{eq}\left(\frac{(1+a)(c_0|_{y=0}-c_{eq})+(b+y)\frac{\partial c_0}{\partial y}|_{y=0}}{c_{eq}}\right) \text{ at } \Sigma_{\beta\gamma} \tag{68}$$

and the problem may be transformed into two independent problems for a and b, i.e., Pb III$_a$ and Pb III$_b$ as presented in Appendix C. It can be noted that $b=-y$ is a solution of Pb III$_b$ and consequently c_i can be simply expressed as

$$c_i = a\left(c_0|_{y=0}-c_{eq}\right)+c_0|_{y=0} \tag{69}$$

Considering $\mathbf{u}_0=\mathbf{u}_i$ and $c_0=c_i$ at $\Sigma_{0,i}$, the mass flux balance described by Eq. (15) can be rewritten as

$$\mathbf{n}_{0,i}\cdot(-D\nabla c_0)=\mathbf{n}_{0,i}\cdot(-D\nabla c_i) \text{ at } \Sigma_{0,i} \tag{70}$$

which can be transformed into

$$\mathbf{n}_{0,i}\cdot(-D\nabla c_0)=-\frac{c_0|_{y=0}-c_{eq}}{A_{0,i}}D\int_{A_{0,i}}\frac{\partial a}{\partial y}dA \text{ at } \Sigma_{0,i} \tag{71}$$

where $A_{0,i}$ is the surface area of the boundary $\Sigma_{0,i}$. For later use, an effective reaction rate coefficient k^0_{eff} is defined as

$$k^0_{\text{eff}}=-\frac{D\int_{A_{0,i}}\frac{\partial a}{\partial y}dA}{A_{0,i}} \tag{72}$$

and the effective boundary condition at Σ_0 can be recast into

$$\mathbf{n}_{0,i}\cdot(-D\nabla c_0)=-k^0_{\text{eff}}c_{eq}\left(1-\frac{c_0|_{y=0}}{c_{eq}}\right) \quad \text{at } \Sigma_0 \tag{73}$$

Remarkably, *the obtained effective boundary condition is, mathematically speaking, of a reactive type, even in the case with micro-scale thermodynamic equilibrium*. Of course, the effective boundary condition has the same form in case I and case II, but the values of k^0_{eff} are given by closure problems with different boundary conditions, as illustrated in Appendix C.

For Σ_{eff} at an arbitrary position $y=w$, the first order estimate of the macro-scale concentration can be developed as

$$c_0|_{y=w}=c_0|_{y=0}+w\left.\frac{\partial c_0}{\partial y}\right|_{y=0} \tag{74}$$

Assuming at first order that $\frac{\partial c_0}{\partial y}|_{y=w}=\frac{\partial c_0}{\partial y}|_{y=0}$, Eq. (73) is rewritten as

$$D\frac{\partial c_0}{\partial y}|_{y=w}=k^0_{\text{eff}}c_{eq}\left(1-\frac{c_0|_{y=w}-w\frac{\partial c_0}{\partial y}|_{y=w}}{c_{eq}}\right) \text{ at } y=w \tag{75}$$

Therefore, the following reactive condition at an arbitrary effective surface for case I and case II is obtained

$$\mathbf{n}_{0,i}\cdot(-D\nabla c_0)=-k^w_{\text{eff}}c_{eq}\left(1-\frac{c_0|_{y=w}}{c_{eq}}\right) \quad \text{at } \Sigma_{\text{eff}} \tag{76}$$

with

$$k^w_{\text{eff}}=\frac{k^0_{\text{eff}}}{1-\frac{w}{D}k^0_{\text{eff}}} \tag{77}$$

Again, the remarkable result is that, whatever the boundary condition at $\Sigma_{\beta\gamma}$ (i.e., thermodynamic equilibrium or reactive), the effective boundary condition has the same reactive form. However, it is possible to define an effective surface Σ^c_{eff} to recover an equilibrium condition, i.e., $c_0=c_{eq}$. From Eq. (75), the position of this surface is given by

$$w^c_x=\frac{D}{k^0_{\text{eff}}}=-\frac{A_{0,i}}{\int_{A_{0,i}}\frac{\partial a}{\partial y}dA} \tag{78}$$

3.3. Effective surface and effective boundary conditions

After resolution of the closure problems, it has been shown that the boundary condition for the flow problem is of Navier type (results already known) and of Robin type for the mass transfer problem (the original part of this paper). It has also been indicated how to estimate the effective boundary condition for a position of the effective surface different from Σ_0. Nevertheless, the three surfaces defined previously, Σ_0, Σ^v_{eff} and Σ^c_{eff}, are those of main interest as will be discussed in the next sections.

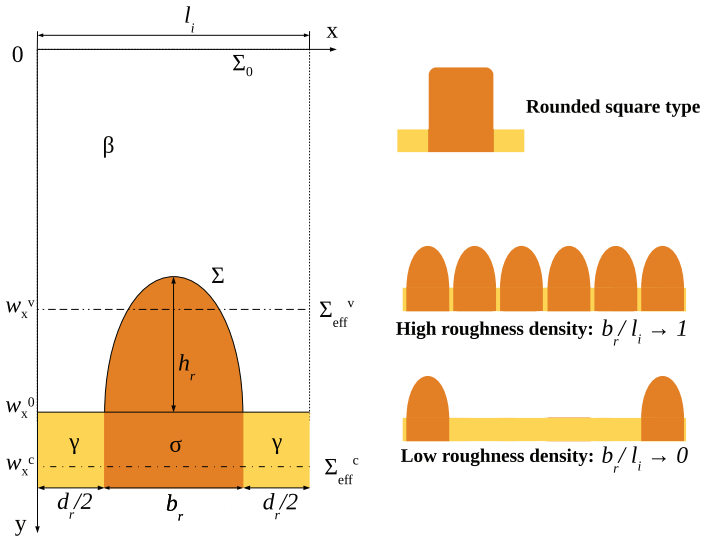

Fig. 5. Unit cell geometry for the simulation (left) and illustration of roughness shape and roughness density (right).

The obtained general form of the effective boundary value problem consists of Pb II and the boundary conditions at the effective surface, for instance, Eqs. (57) and (76) for an arbitrary surface position Σ_{eff} (at $y = w$), which become Eqs. (55) and (73) when the effective surface is at Σ_0, or

$$\begin{cases} \mathbf{u}_i = 0 \\ -\mathbf{n}_{ls} \cdot D\nabla c_0 = -k_{\text{eff}}^v c_{eq} \left(1 - \frac{c_0}{c_{eq}}\right) \end{cases} \tag{79}$$

when the effective surface is at Σ_{eff}^v, or

$$\begin{cases} \mathbf{u}_i = \left(w_x^c - w_x^v\right) \frac{\partial u_0}{\partial y}\big|_{y=0} \mathbf{e}_1 \\ c_0 = c_{eq} \end{cases} \tag{80}$$

when the effective surface is at Σ_{eff}^c.

4. Effective parameters calculations

The aim of this section is to analyze the impact of some factors, for instance the roughness features, the Péclet, the Schmidt and the mean Damköhler numbers, on the effective parameters. The Péclet and the Schmidt numbers are defined as

$$\text{Pe}_l = \frac{u_{ref} w_x^0}{D}, \quad \text{Sc} = \frac{\mu}{\rho D} \tag{81}$$

where, the cell height w_x^0 is used as a characteristic length. The reference flow velocity u_{ref} is chosen as the x-component of the velocity at Σ_0. The mean Damköhler number will be defined later.

Dimensionless forms of closure problem Pb $\text{III}_{(\mathbf{B},s)}$ and Pb III_a are solved to obtain the effective surface position and boundary conditions, with the unit cell presented in Fig. 5. Two shapes of roughness are used in the simulations, semi-ellipse or rounded square. The height of the roughness h_r and its width b_r are the two independent parameters. The height and width of the unit cell are denoted as w_x^0 (with $w_x^0 = 8h_r$) and l_i, respectively. In the following simulations, w_x^0 and h_r have fixed values, while l_i and b_r are varied in order to modify either the roughness geometry or the roughness density as shown in Fig. 5.

All the following simulations are performed using COMSOL®. The linear systems are solved with the direct solver UMFPACK, which is based on the Unsymmetric MultiFrontal method. The velocity field in Pb III_a is calculated by solving dimensionless steady-state Navier–Stokes equations. Quadratic Lagrange element formulation is used for the closure variables a, $\mathbf{B}$ and the velocity. Linear Lagrange element settings are used for pressure and its mapping variable s. Proper mesh qualities are obtained to ensure convergence. For example for the unit cell with $\frac{b_r}{l_i} = 0.1$, $\text{Pe}_l = 25$ and $\text{Sc} = 1$, since further increase of the number of degrees of freedom larger than 10^4 leads to the variation of $\int_{A_{0,i}} \frac{\partial a}{\partial y} dA$ less than 1%, it is considered that the results are of appropriate quality in such circumstances. Given the fact that the unit cell geometry under study is quite simple, it is very easy to get converged results; therefore no more details of the procedure are provided here. An example of the converging process is given in the Supporting Information.

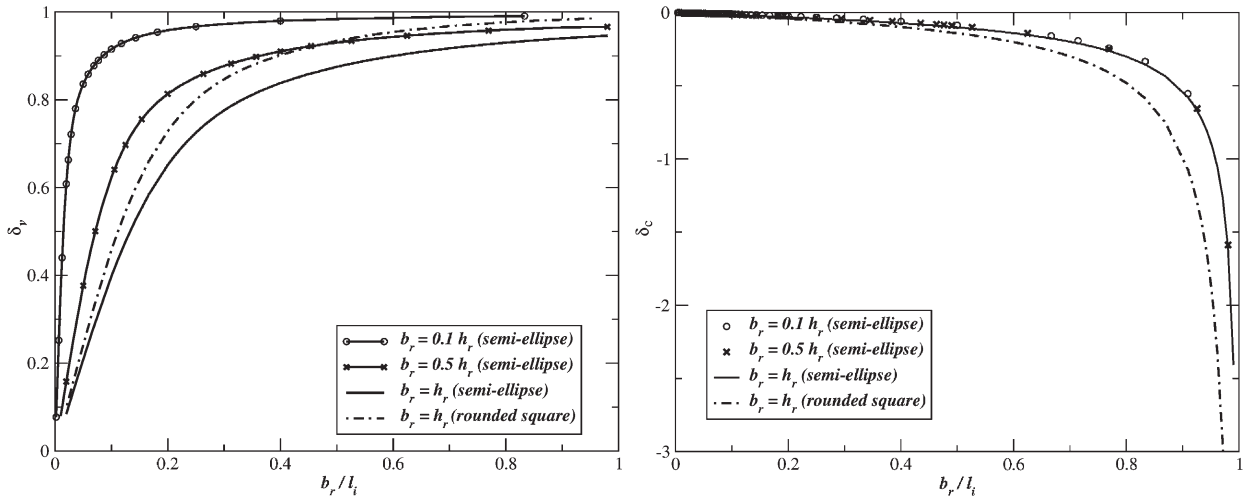

Fig. 6. Effective surface position of Σ^v_{eff} (left) and Σ^c_{eff} (right) for different roughness geometries and densities.

4.1. Effect of roughness features on effective surface positions

In this subsection the influences of the roughness geometry and density on the positions of Σ^v_{eff} and Σ^c_{eff} are investigated. Since w^v_x and w^c_x are values varying with the choice of Σ_0, it is more convenient to introduce the corresponding normalized values $\delta_v = \frac{w^0_x - w^v_x}{h_r}$ and $\delta_c = \frac{w^0_x - w^c_x}{h_r}$ to indicate the effective positions relative to the solid surface (see Fig. 4, where δ_v and δ_c are not normalized with respect to h_r). Results for four sets of simulations are presented in Fig. 6.

In the left graph, it is observed that both the geometry and the roughness density have an impact on δ_v. One can observe that for higher roughness densities, i.e., $\frac{b_r}{l_i} \to 1$, Σ^v_{eff} goes closer to the roughness height because the narrow gaps between asperities make it difficult for the fluid to flow through. The upper limit of δ_v is one and is nearly reached for the thin semi-ellipse and the rounded squares because their roughness shapes are steep. For roughnesses close enough to each other, the heterogeneous surface has a similar behavior in terms of momentum transport as a smooth surface located at the height of the roughnesses. For smoother roughnesses, the limit case where two roughnesses are adjacent gives a value of δ_v smaller than one as the fluid can still flow partially between the roughnesses. The three sets of simulations with semi-ellipse shape also show that thin roughnesses create more resistance to the flow than wider ones. The curves exhibit another limit when $\frac{b_r}{l_i} \to 0$. Even if the two neighboring asperities are far enough from each other, e.g., $l_i = 50h_r$ in this case, the roughnesses still have some small impact on the flow and δ_v tends towards $0.1h_r$.

In the right graph of Fig. 6, the negative values of δ_c mean that Σ^c_{eff} locates inside the solid part. The presence of insoluble materials makes the averaged concentration on Σ smaller than the equilibrium concentration, therefore Σ^c_{eff} must be located beneath Σ to recover the thermodynamic equilibrium. Similar to the case with no-slip condition, both roughness shape and roughness density are playing a role on δ_c. However, one can observe that the three sets of simulations with semi-ellipse shapes are superposed, indicating that the width of the roughness has little impact on δ_c for a given ratio of $\frac{b_r}{l_i}$. One sees from these results that δ_c tends towards $-\infty$ when the ratio $\frac{b_r}{l_i}$ increases towards one, independently of the roughness geometry. For $\frac{b_r}{l_i} \to 1$, the solid surface in contact with the fluid is mainly formed by the insoluble material and little mass transfer occurs between the solid and the fluid, which makes it difficult to recover thermodynamic equilibrium effective boundary condition. The upper limit of δ_c is equal to zero and is obtained for low roughness density ($\frac{b_r}{l_i} \to 0$). In this case the solid–liquid interface behaves like a homogeneous soluble surface.

4.2. Thermodynamic equilibrium case (B.C. I)

In this subsection, the dependence of k^v_{eff} on different factors is investigated first. Simulations are conducted for both advective–diffusive mass transport regime and purely diffusive regime. In the latter case, the effective reaction rate coefficient is denoted as $k^v_{\text{eff}_{\text{diffu}}}$. The flat part of the solid–liquid interface is under thermodynamic equilibrium. The roughness shape is semi-ellipse with a height of h_r. The other geometric parameters of the unit cell are $w^0_x = 8h_r$, $b_r = 0.5h_r$ and $l_i = 5h_r$.

The ratio of $\frac{k^v_{\text{eff}}}{k^v_{\text{eff}_{\text{diffu}}}}$ as a function of Pe_l and Sc is plotted in Fig. 7.

One sees in the figure that $\frac{k^v_{\text{eff}}}{k^v_{\text{eff}_{\text{diffu}}}}$ increases globally with Pe_l and Sc, which means that the flow has a stronger impact on mass transport, as advection becomes more important when increasing (Pe_l, Sc). For all tested Sc, when $\text{Pe}_l < 10$, the

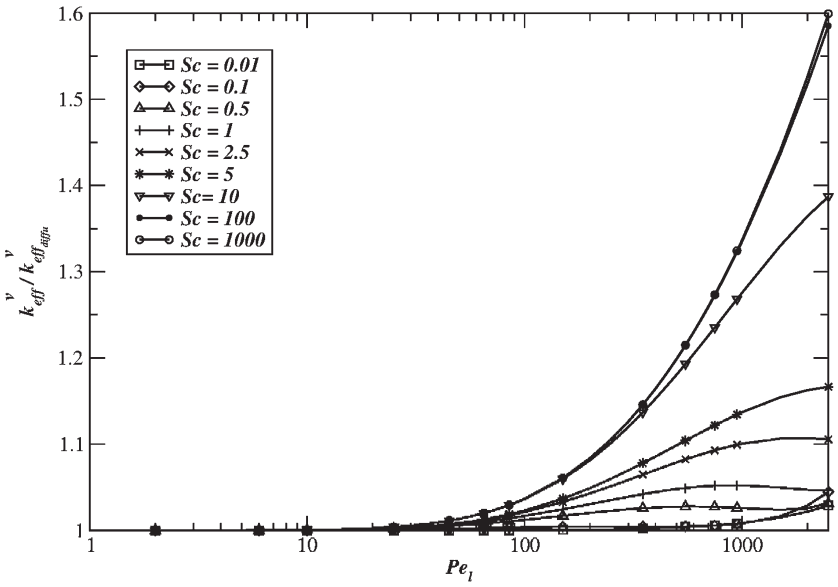

Fig. 7. Ratio between k^v_{eff} with advection and its value in the purely diffusive case, as a function of Pe_l and Sc. Semi-ellipse roughness was used with $b_r = 0.5h_r$ and $\frac{b_r}{l_i} = 0.1$.

effective reaction rate coefficient with advection is nearly the same as the one under a purely diffusive regime. For $\text{Sc} < 0.1$, the difference between k^v_{eff} and $k^v_{\text{eff}_{\text{diffu}}}$ is less than 1% for $\text{Pe}_l < 1000$. Consequently, the mass transport problem can be simplified into a pure diffusion case in such circumstances, producing an error smaller than 1%. For the cases with Sc close to 1, $\frac{k^v_{\text{eff}}}{k^v_{\text{eff}_{\text{diffu}}}}$ reaches a maximum at high Pe_l values, then decreases and increases again. For higher Sc the ratio increases with Pe_l with different rate except for $\text{Sc} = 100$ and $\text{Sc} = 1000$ that are superposed on the studied range of Pe_l. One has to pay attention that the considered situation in this study is laminar flow within a boundary layer. Therefore for the cases with small Sc, the considered Pe_l should not be too large.

To illustrate the different regimes between mass transport governed by diffusion or by advection, the streamlines of the total flux of a versus Sc and Pe_l are plotted in Fig. 8. With small Pe_l (10 and 50), the variation of Sc only has some small impact on the streamlines, which illustrates the weak influence of the flow on the mass exchange at the reactive surface. The value of k^v_{eff} is therefore close to the value in the purely diffusive case (with a difference less than 1%) as illustrated in Fig. 7. With larger Pe_l values, increasing Sc (i.e., increasing the viscosity) delays the occurrence of recirculations close to the rough surface, which explains the maximum values observed in Fig. 7. The recirculations first limit mass transport towards the soluble material, and then enhance it for increasing Pe_l, corresponding to the decrease and increase of $\frac{k^v_{\text{eff}}}{k^v_{\text{eff}_{\text{diffu}}}}$ after the maximum values.

In a second set of simulations, the influence of the rough surface geometry on $\frac{k^v_{\text{eff}}}{k^v_{\text{eff}_{\text{diffu}}}}$ is investigated by changing the roughness density. From the results presented in Fig. 9, a high roughness density leads to a delay in the transition between the advective and diffusive regime. One can observe for example that for $\frac{b_r}{l_i} = 0.4$ and $\frac{b_r}{l_i} = 0.5$, the flow alone has a small impact on the effective reaction rate coefficient (less than 1%) even for high Pe_l values. In these configurations, $k^v_{\text{eff}_{\text{diffu}}}$ is a good estimate of k^v_{eff}. As the roughness density decreases, $\frac{k^v_{\text{eff}}}{k^v_{\text{eff}_{\text{diffu}}}}$ increases because the flow can pass through the roughness more easily, and therefore more solid surface under thermodynamic equilibrium is available for mass transfer.

4.3. The case of a reactive surface (B.C. II)

In this subsection, the flat part of the solid–liquid interface is reactive. To study the impact of the chemical features on the effective reaction rate coefficient, some parameters are first introduced. Let k_σ denote the reactivity at surface $\Sigma_{\beta\sigma}$. One should note that k_σ is equal to zero in this study since the σ-phase is non-reactive. The surface average reaction rate coefficient for a heterogeneous surface can be approximated as $\hat{k} = \frac{k_\gamma A_{\beta\gamma} + k_\sigma A_{\beta\sigma}}{A_{\beta\gamma} + A_{\beta\sigma}}$, with $A_{\beta\gamma}$ and $A_{\beta\sigma}$ representing the surface areas of $\Sigma_{\beta\gamma}$ and $\Sigma_{\beta\sigma}$, respectively. According to the mass conservation from Σ to Σ^v_{eff}, the surface average reaction rate coefficient at Σ^v_{eff} can be estimated as $\hat{k}^v = \frac{k_\gamma A_{\beta\gamma} + k_\sigma A_{\beta\sigma}}{A_v}$, with A_v denoting the surface area of Σ^v_{eff}. The structure of the concentration field inside the domain will depend on the ratio between reaction characteristic rates and diffusion, corresponding to a mean Damköhler number defined as $\widehat{\text{Da}} = \frac{\hat{k} w_x^0}{D}$.

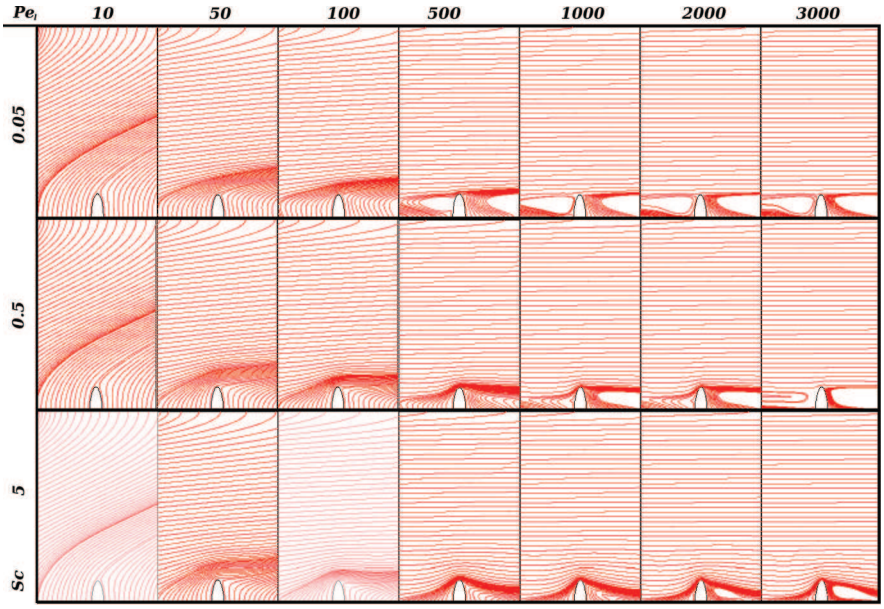

Fig. 8. Total flux streamlines of closure variable a for different Sc and Pe_l. The roughness shape is a semi-ellipse with $b_r = 0.5h_r$ and $\frac{b_r}{l_i} = 0.1$.

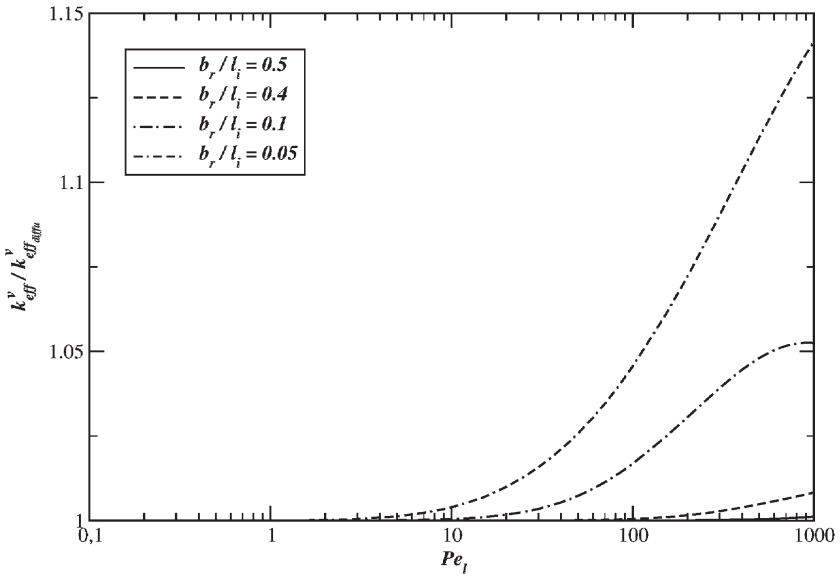

Fig. 9. Ratio between k^v_{eff} with convection and its value in the purely diffusive case, as a function of the local Péclet number, for different roughness densities given by $\frac{b_r}{l_i}$ and $\mathrm{Sc} = 0.1$.

The roughness shape under consideration is semi-ellipse. The height and width of the roughness, as well as the height of the unit cell remain unchanged, with $b_r = 0.5h_r$ and $w_x^0 = 8h_r$. Two roughness densities, $l_i = 5h_r$ and $l_i = 10h_r$, are considered.

The results of $\frac{k^v_{\mathrm{eff}}}{\hat{k}^v}$ versus $\widehat{\mathrm{Da}}$ are presented in Fig. 10 for different Pe_l and Sc. For small $\widehat{\mathrm{Da}}$, $\frac{k^v_{\mathrm{eff}}}{\hat{k}^v}$ tends towards one despite of the flow properties. In such circumstances, the characteristic time of reaction is long compared to the mass-transfer kinetics, and the process is consequently limited by reaction. With the increase of $\widehat{\mathrm{Da}}$, mass transfer becomes insufficient and the process is therefore limited by the mass transport. In other words, $\hat{k}^v$ tends to infinity while k^v_{eff} remains a constant, leading to $\frac{k^v_{\mathrm{eff}}}{\hat{k}^v}$ tending towards zero.

For a fixed roughness density, $l_i = 5h_r$ or $l_i = 10h_r$, when $\mathrm{Pe}_l = 1$, an increase of Sc does not affect $\frac{k^v_{\mathrm{eff}}}{\hat{k}^v}$ since the curves of $\mathrm{Sc} = 1$ and $\mathrm{Sc} = 1000$ are superposed, while when Sc remains unchanged, the increase of Pe_l delays the decrease of $\frac{k^v_{\mathrm{eff}}}{\hat{k}^v}$.

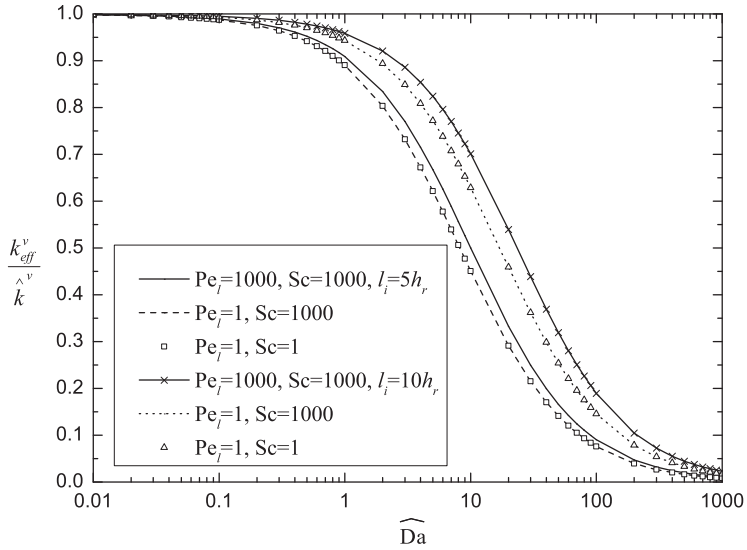

Fig. 10. The ratio of effective reaction rate coefficient k^v_{eff} over the surface average reaction rate coefficient $\hat{k}^v$, as a function of the mean Damköhler number, with different surface geometries.

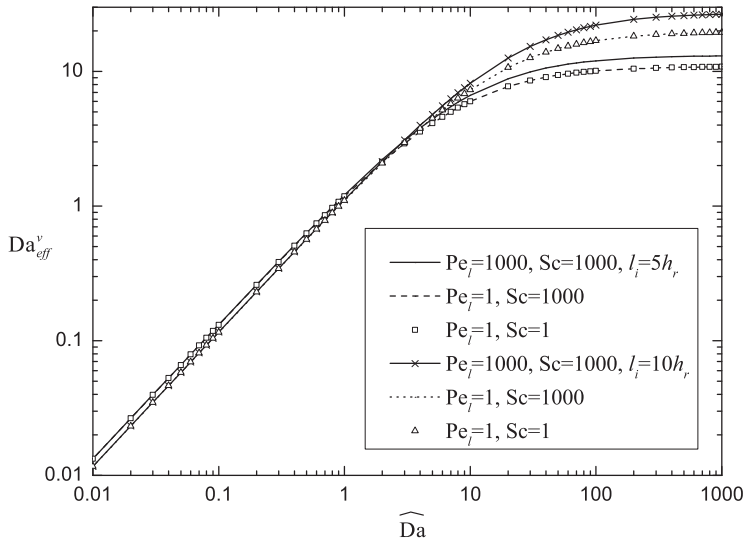

Fig. 11. The functionality of the effective Damköhler number $\mathrm{Da}^v_{\mathrm{eff}}$ with the mean Damköhler number $\widehat{\mathrm{Da}}$.

These results illustrate that only relatively large Pe_l have some impact on k^v_{eff}, consistent with the following discussion about $\mathrm{Da}^v_{\mathrm{eff}}$ and with the results illustrated later by Fig. 12. For the geometry with $l_i = 10h_r$, the decrease of $\frac{k^v_{\mathrm{eff}}}{\hat{k}^v}$ is delayed since the fluid can flow through the roughness more easily thus enhance mass transfer. Therefore, it can be concluded that the roughness density, the flow properties in terms of Pe_l and the chemical features in terms of $\widehat{\mathrm{Da}}$ have an important influence on k^v_{eff}.

Since it is not convenient to use the ratio $\frac{k^v_{\mathrm{eff}}}{\hat{k}^v}$ when $\widehat{\mathrm{Da}}$ is large because it tends to zero, an effective Damköhler number defined as $\mathrm{Da}^v_{\mathrm{eff}} = \frac{k^v_{\mathrm{eff}} w^0_x}{D}$ is introduced to indicate the evolution of k^v_{eff} with $\widehat{\mathrm{Da}}$. Results are plotted in Fig. 11. $\mathrm{Da}^v_{\mathrm{eff}}$ is proportional to $\widehat{\mathrm{Da}}$ before it reaches a plateau when mass transport becomes the limiting factor of the chemical process, consistent with the results of a similar analysis in [14]. Quantitatively, when Pe_l remains unchanged, $\mathrm{Da}^v_{\mathrm{eff}}$ for $l_i = 10h_r$ is twice as large as for $l_i = 5h_r$ in the limit of large $\widehat{\mathrm{Da}}$. This is also explained by the fact that mass transport is limiting the process under large $\widehat{\mathrm{Da}}$ and increasing the proportion of the dissolving phase is equivalent to increasing mass transport. Moreover, flow and roughness density have only a small impact on $\mathrm{Da}^v_{\mathrm{eff}}$ for small $\widehat{\mathrm{Da}}$ because in such circumstances it is the surface reaction rate coefficient but not mass transport that controls the process. Furthermore, $\mathrm{Da}^v_{\mathrm{eff}}$ increases with

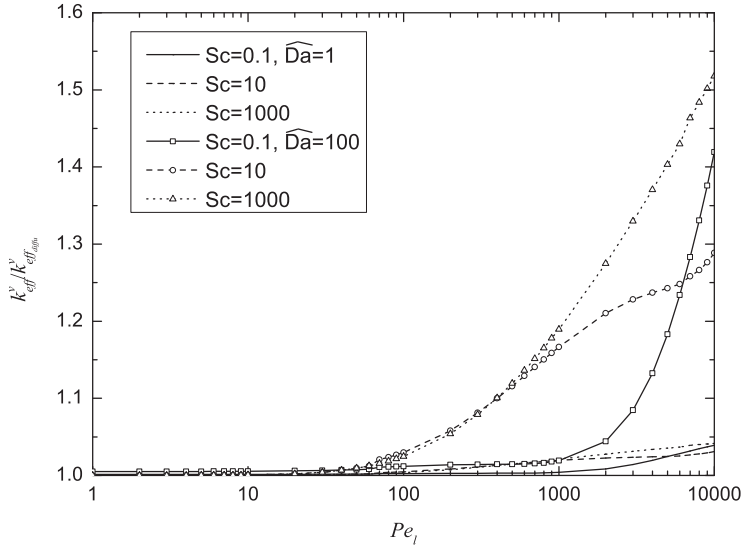

Fig. 12. Ratio between k^v_{eff} with advection and its value in the purely diffusive case, as a function of the local Péclet number and for different Schmidt numbers. The roughness shape is a semi-ellipse with $b_r = 0.5h_r$ and $\frac{b_r}{l_i} = 0.1$.

roughness density under small $\widehat{\text{Da}}$ and decreases with roughness density under large $\widehat{\text{Da}}$, which is due to the transition of the limiting factor.

Finally, the importance of mass transport by advection is studied by plotting $\frac{k^v_{\text{eff}}}{k^v_{\text{eff}_{\text{diffu}}}}$ versus Pe_l for two $\widehat{\text{Da}}$ values and for different Sc, as shown in Fig. 12. One sees from the figure that with the increase of Pe_l, the ratio $\frac{k^v_{\text{eff}}}{k^v_{\text{eff}_{\text{diffu}}}}$ tends to increase since the advection term becomes more important. The curves with the same Sc have similar trends but with different magnitudes. In the case with higher $\widehat{\text{Da}}$, the role of advection is more important and the transitions from the diffusive regime to the advective regime take place at smaller Pe_l. For the curves with $\text{Sc} = 0.1$, the increases happen at relatively large Pe_l and can lead to larger $\frac{k^v_{\text{eff}}}{k^v_{\text{eff}_{\text{diffu}}}}$ than the curves with $\text{Sc} = 10$ in some circumstances, because the growth of $\frac{k^v_{\text{eff}}}{k^v_{\text{eff}_{\text{diffu}}}}$ with $\text{Sc} = 10$ slows down at about $3000 < \text{Pe}_l < 7000$. This trend is similar to the results obtained with the thermodynamic equilibrium boundary condition. Recirculations close to the rough surface have a similar impact, first limiting the mass transport towards the reactive surface and then enhancing it. To summarize, to estimate k^v_{eff} by $k^v_{\text{eff}_{\text{diffu}}}$ will produce an error less than 5% for the studied cases with $\widehat{\text{Da}} = 1$, because the reaction rate coefficient is the limiting factor of process and the flow properties have negligible impact. One has to be careful to represent k^v_{eff} by $k^v_{\text{eff}_{\text{diffu}}}$ at large $\widehat{\text{Da}}$ since the flow properties can have significant influence in such conditions.

5. Application of the effective surface model

As introduced in Section 3, there are different potential choices for the position of the effective surface, e.g., the fictive surface Σ_0, surface Σ^v_{eff} which recovers the no-slip boundary condition, surface Σ^c_{eff} which recovers the thermodynamic equilibrium condition, or any arbitrary location. In this section the objective is to identify the most appropriate effective surface by investigating the errors between direct numerical simulations (DNSs) over the original rough surface and simulations with the effective surface model. Two situations are considered, typical of the development of a mass boundary layer over a rough surface.

The first application corresponds to a boundary layer over a rough wall parallel to the flow. The original model for DNSs is illustrated by the upper drawing of Fig. 13(a). The characteristic length of the system used to normalize the space variables is H_Ω, i.e., L, the height of the global domain. The system is $W = 3H_\Omega$ wide. A short flat zone is set with a length of $0.5H_\Omega$ before the rough surface in order to have an already developed boundary layer, which is closer to the periodic boundary condition hypothesis stated previously. In addition, the roughness height is chosen to be small enough to have $\epsilon = \frac{l}{L} = 0.1$ and $l = 8h_r$. The roughness has a shape of semi-ellipse with $b_r = 0.5h_r$. In terms of geometry for the effective models, the flat surface at the entrance remains unchanged and the original rough surface is replaced by a smooth effective one. The lower drawing in Fig. 13(a) gives an example of the effective model with no-slip condition at the effective surface. The original flat surface and the effective surface are connected by a small step. It is clear that some assumptions of the homogenization are not valid in this particular area, which is a singularity (no-periodicity, etc.). Specific developments could be done to overcome this problem, but in the present work the general results are simply used to see if it is acceptable.

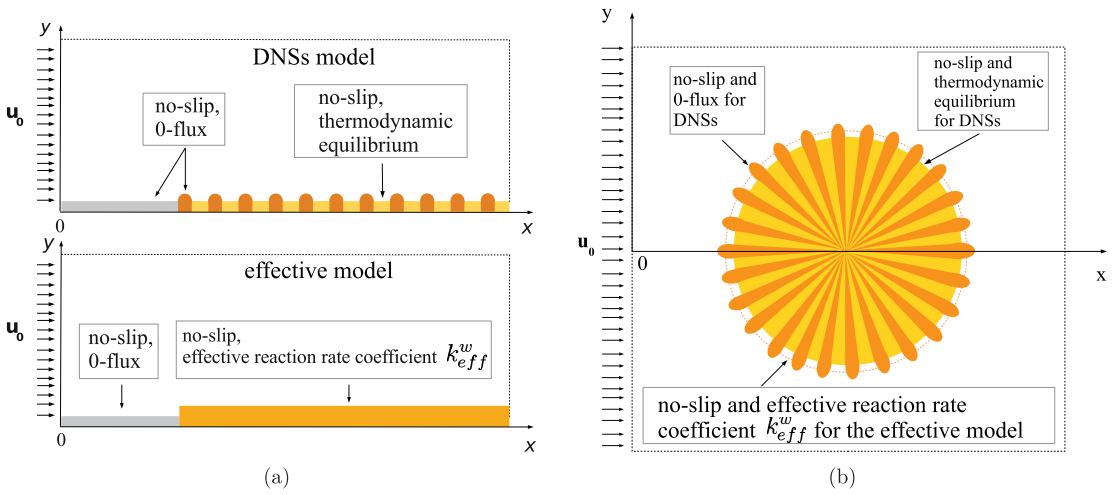

Fig. 13. Schematic representation of the computational domain: DNSs over the heterogeneous surface and the first order effective models (application 1 in (a) and application 2 in (b)).

In the second application, the boundary layer develops on a rough cylinder perpendicular to the flow. As illustrated in Fig. 13(b), the rough surface in the DNSs is replaced by the smooth circular surface in the effective model. Since the considered geometry is symmetric with respect to x-axis, only the transport in the upper half domain is simulated. The characteristic length of the system used to normalize the space variables is L, the cylinder diameter. The height of the half domain is $H_\Omega = 1.5L$ and the width is $W = 2.5L$.

DNSs are performed using dimensionless forms of Pb I equations with B.C. I. For the effective model, the closure problems Pb III$_{(\mathbf{B},s)}$ and Pb III$_a$ illustrated in the appendices are solved first to obtain the effective surface position and the effective boundary conditions, as summarized in subsection 3.3. Then the effective macro-scale problem Pb II is solved using these obtained effective boundary conditions. Similar numerical settings were used as in the last section. Convergence analyses were conducted for each computation to guaranty the results quality (see Support Information).

5.1. Application 1: boundary layer over a rough wall parallel to the flow

The way to quantify the differences between the two simulations is to calculate the error on the integration of the total mass flux over the solid–liquid surface, called Q_{DNS} for the rough surface and Q_{eff} for the effective one. Simulations are done for flows with $\text{Re}_L = 1$ and $\text{Re}_L = 50$, with two roughness densities: $\frac{h_r}{l_i} = 0.5$ and $\frac{h_r}{l_i} = 0.1$. The relative errors on the total mass flux are plotted in Fig. 14 for different effective surface positions. For effective surface at a position lower than $2.5h_r$, the relative error committed by the model is smaller than 1%. At higher effective surface positions and for the different Reynolds numbers, the error increases when increasing the position of the effective surface. One can also observe that the roughness density has little impact on the error compared to the influence of Re_L. Increasing the distance between roughnesses by a factor of five only increases the error by less than 1%, while increasing Re_L from 1 to 50 nearly doubles the error. For the different flow conditions or geometry, a minimum value of the relative error is obtained around $y_{\text{eff}} = h_r$. It is closest to Σ^v_{eff} among the particular effective surface positions discussed before.

To demonstrate the representativeness of the effective model with the effective surface located at Σ^v_{eff}, the results of DNSs and the first order effective model are compared in terms of velocity, concentration fields and the distribution of mass flux over the reactive surface as illustrated in Figs. 15 and 16, respectively. Results with the effective surface at Σ_0 are also shown in these figures to illustrate the discrepancies created by the large step between the flat zone and the effective surface.

In the upper graph of Fig. 15, one can observe that the velocity contours obtained by DNSs (solid line) and those obtained with the first order effective model with an effective surface at $\frac{w^0_x - w^v_x}{L}$ i.e., at Σ^v_{eff}, are overlapped, with negligible errors. This is consistent with previous findings in the literature for the momentum transport problem. Results with the effective surface at $\frac{w^v_x}{L}$ (dot line), i.e., at Σ_0, give the good trend but are not precisely representing the DNSs velocity field. As for concentration contours, one sees in the lower graph of Fig. 15 that those obtained with the effective surface at $\frac{w^0_x - w^v_x}{L}$ are also well superposed with the DNSs results, except inside the small entrance region where the conditions for upscaling break down as discussed previously. Quantitatively, this creates a small and rather acceptable discrepancy of 0.07% on the total mass flux. The iso-concentration contours obtained with the effective surface at $\frac{w^0_x}{L}$ show some discrepancies that increase with $\frac{x}{L}$, leading to a relative error on the total mass flux of around 6.2%.

In Fig. 16, the distribution of the normal mass flux, q, along the reactive surfaces in the effective model with Σ^v_{eff} and Σ_0 and that along the rough surface in the original model are compared. For the DNSs, values are discrete because q needs

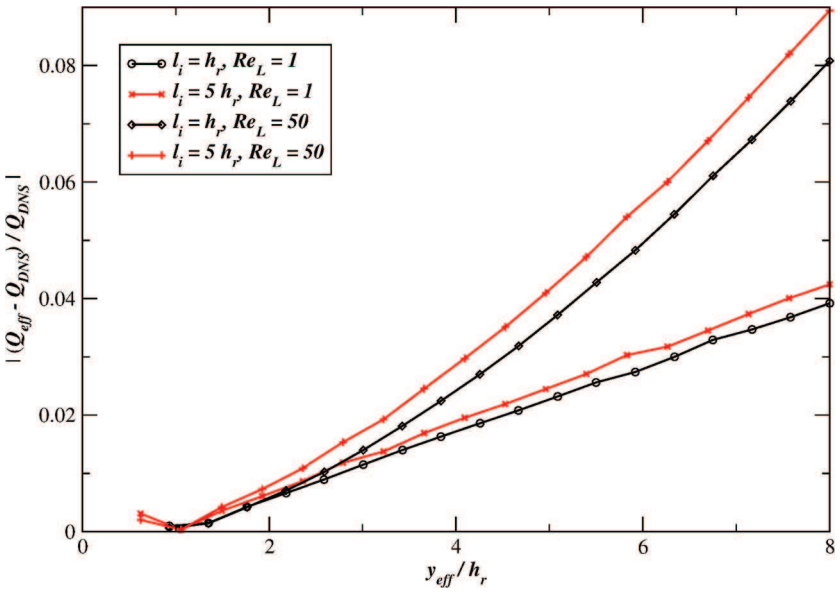

Fig. 14. Relative error on Q_{eff} compared to Q_{DNS}, for different positions of the effective surface, with different surface geometries, $Sc = 1$ and two values of Re_L.

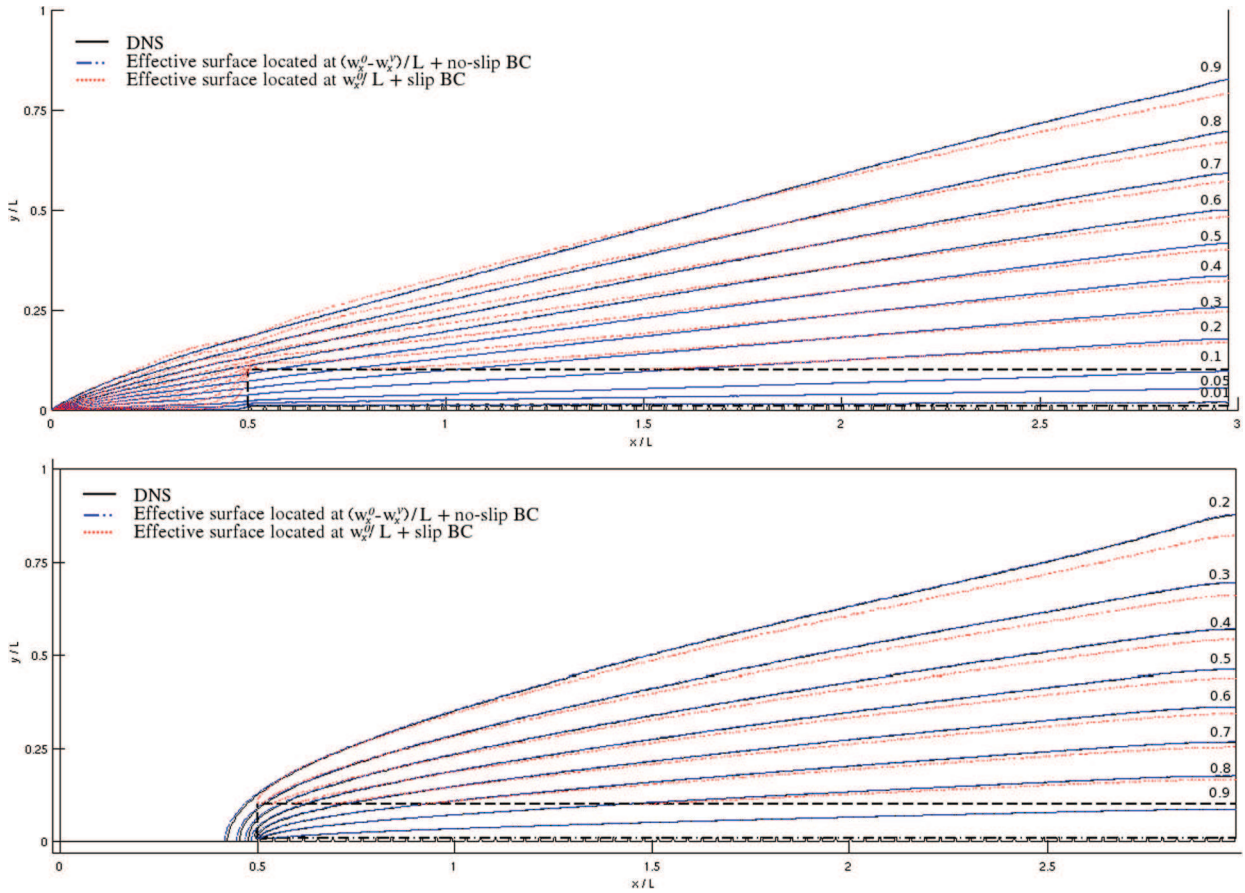

Fig. 15. Dimensionless velocity field (upper graph) and concentration (lower graph) contours for the initial rough domain and two effective smooth domains, with an entrance dimensionless flow velocity of 1, $Re_L = 25$ and $Sc = 1$.

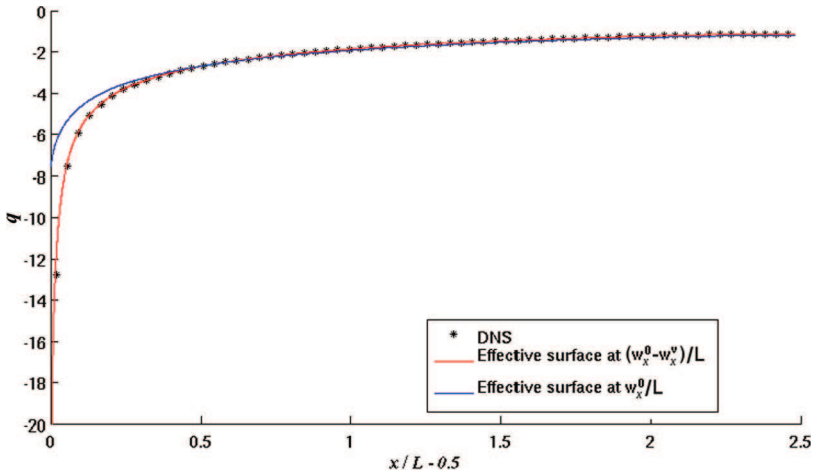

Fig. 16. Normal flux along the reactive surfaces for the initial rough domain and two effective smooth domains, with an entrance dimensionless flow velocity of 1, $\mathrm{Re}_L = 25$ and $\mathrm{Sc} = 1$.

to be averaged for each l_i. The results of the DNSs and the effective model with Σ^v_{eff} show a good agreement. For the model with the effective surface at Σ_0, q distribution differs from the DNSs in the entrance region after the step. This is mainly the consequence of the discrepancies observed in the velocity field.

5.2. Application 2: rough cylinder in a laminar flow

This second case illustrates the accuracy of the effective model for a more complex configuration than the previous application. Simulations are done for a flow with $\mathrm{Re}_L = 0.1$ and $\mathrm{Sc} = 1000$, with 50 roughnesses distributed uniformly over the cylinder surface and $\epsilon = 0.1$. In the two graphs of Fig. 17, one can observe that both velocity contours (top) and concentration contours (bottom) obtained by DNSs (black solid line) and with an effective surface at Σ^v_{eff} (blue dashed line) are overlapped, with negligible errors. The error on Q is less than 0.1%, proving again the validity of the first order effective surface model. This error remains smaller than 0.1% even by increasing ϵ to 0.5 (the scale separation assumption is no more valid). However for $\mathrm{Re}_L = 1$, $\mathrm{Sc} = 1000$ and $\epsilon = 0.5$, the model starts to show some limitations and gives results with an error around 3%.

5.3. Effective parameters estimates

In these last paragraphs, potential estimates of the effective properties are discussed in order to reduce computational costs, taking application 1 as an example. As mentioned previously in Section 4, for a high roughness density the effective surface position is close to the roughness height. One first possible approximation is to set the effective surface position at the roughness height, using a no-slip boundary condition and then use the effective reaction rate obtained for an effective surface at h_r, which will be called Σ^r_{eff}. Relative errors committed on the total mass flux using this approximation are compared to the one with the correct effective model with Σ^v_{eff}. Results are assembled in Table 1 for $\mathrm{Re}_L = 25$ and $\mathrm{Sc} = 1$, and for rounded square roughnesses with $b_r = h_r$. The approximated model gives results with relative errors less than 1% even for roughness densities as low as 0.2, i.e., $\frac{b_r}{l_i} = 0.2$ with $\delta_v = 0.73$. This first approximation gives good results for certain rough surface geometries and will save computational time as the closure problem for the flow does not need to be solved anymore.

In addition to this first estimate, an approximation can be made on the effective reaction rate as well. In the range of Re_L used for the global simulations (1 to 1000), the corresponding micro-scale Péclet number will not exceed 100 for Schmidt numbers below 10. From the parametric study of Section 4, it has been observed that the effective reaction rate obtained for pure diffusion can be a good approximation of the effective reaction rate with flow. As a result, Pb III_a with B.C. I can be simplified into a purely diffusive one in these application ranges. For example, the largest difference between errors on Q, committed with and without accounting for the flow in k^v_{eff} is 0.002 (obtained with $\frac{b_r}{l_i} = 0.1$, $\mathrm{Re}_L = 500$ and $\mathrm{Sc} = 5$ which has a ratio $\frac{k^v_{\mathrm{eff}}}{k^v_{\mathrm{eff}_{\mathrm{diffu}}}} \approx 1.02$).

To sum up, all these numerical results demonstrate the efficiency of using an effective surface model, characterized by a homogeneous and smooth surface, to reproduce the flow and reactive mass transport over a heterogeneous rough surfaces, with a good accuracy. The use of estimates without solving Pb $\mathrm{III}_{(\mathbf{B},s)}$ can help to gain computational time, but may need to be tested on larger domains.

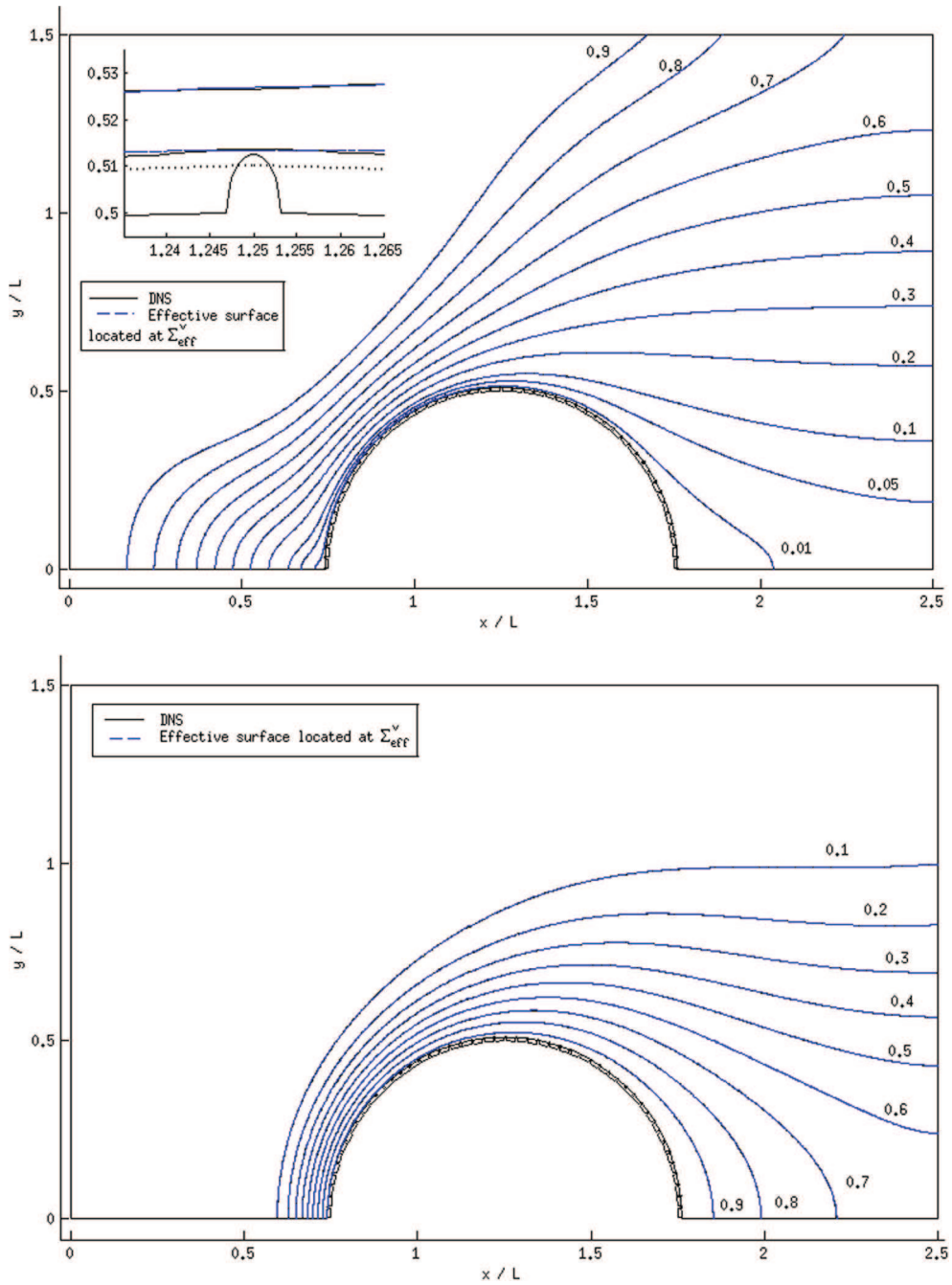

Fig. 17. Dimensionless velocity field (top) and concentration (bottom) contours for the initial rough domain and the effective smooth domain, with an entrance dimensionless flow velocity of 1, $Re_L = 0.1$ and $Sc = 1000$.

6. Conclusion

The concept of effective surface has already proven its usefulness for several transport mechanisms. The main contribution of this paper concerns mass (and momentum) transfer for a laminar flow over a heterogeneous rough surface characterized by *mixed* boundary conditions. A very important constraint necessary to develop the effective surface concept is the separation of scales between the global boundary layer thickness and the zone of influence of the surface heterogeneities within that boundary layer. Additional assumptions were made, like micro-scale pattern periodicity, which could probably be replaced by less restrictive constraints. Based on these assumptions, the methodology of multi-domain decom-

Table 1
Relative errors committed on the total mass flux over the reactive surface between the effective model simulations and the DNSs, for different roughness densities with $b_r = h_r$ and rounded square roughnesses, an entrance dimensionless flow velocity of 1, $\mathrm{Re}_L = 25$ and $\mathrm{Sc} = 1$.

$\frac{b_r}{l_i}$	δ_v	Σ^v_{eff} (in %)	Σ^r_{eff} (in %)
0.8	0.977	0.262	0.179
0.67	0.964	0.234	0.117
0.2	0.729	0.372	0.674
0.1	0.458	0.581	1.63
0.067	0.318	0.675	2.03

position was used to decompose the domain under investigation into a macro-scale subdomain and a range of micro-scale unit cells.

To determine what boundary conditions should be prescribed and where the effective surface should be placed, first order estimates of the micro-scale variables were made by means of Taylor expansion, and the resolution was obtained by solving corresponding closure problems. After this homogenization procedure, alternative effective surface positions were found. General expressions for the effective boundary conditions were obtained, and, for some effective surfaces of interest, the related effective boundary conditions were derived from the generic form. Among the different choices, the effective surface with a no-slip boundary condition or any other position close to this surface have the advantage that it induces the smallest errors. For a rough surface with part under equilibrium and part with no flux, the effective boundary condition turns out to be of a *reactive type*, with an effective reaction rate coefficient depending on the geometry and flow properties. Interestingly, this establishes a fundamental relationship with the case of a reactive surface with non-uniform reaction rates ([30] and this paper).

The influences of some parameters, including roughness geometry, flow properties and surface chemical characteristics, were studied. These analyses showed that the geometry of the asperities, in terms of density and shape, has a significant impact on the effective surface position. A higher roughness density leads to an effective surface farther from the lower part of the rough surface, and vice versa. Flow properties have a stronger impact for the case with smaller roughness density.

The study of the impact of flow properties showed that in some circumstances, the advective–diffusive flow regime can be simplified into a purely diffusive one. In addition, since the chemical characteristics are the limiting factors at small $\widehat{\mathrm{Da}}$, it is acceptable to approximate the effective reaction rate coefficient by the surface average. At large $\widehat{\mathrm{Da}}$, the chemical process is controlled by the mass transport, and the effective reaction rate coefficient should be calculated by the closure problems developed for the specific conditions. Due to the strong impact of flow properties at large $\widehat{\mathrm{Da}}$, the mass transport by advection should be taken into account.

At last, simulations were conducted for both the original model and the effective ones in application 1. The results comparison in terms of total flux showed that the one with the no-slip condition (Σ^v_{eff}) is more accurate than the fictive surface with slip condition (Σ_0). Contours of velocity and concentration, and total flux at a specific cross-section obtained by the original model and by the effective model with the effective surface at Σ^v_{eff} agreed very well. Velocity and concentration comparisons for a more complex geometry also showed good agreements. These two applications demonstrate the representativeness of the effective surface models to the original ones.

As indicated in the introduction, one of the motivation for this study was to model phenomena taking place at "dissolving" interfaces (drying, karstic and other underground cavities, etc.). Therefore, the surface geometry is not given a priori but is a result of the process. How the surface geometry changes with time under different conditions? What is the recession rate? And how these effects can be handled by a macro-scale theory (here the concept of effective surface) are open problems which are of major interest. Additional coupling may arise, in particular, hydrodynamic and dissolution instabilities may produce different surface patterns (as illustrated in [23]) and this also is an issue that needs to be considered in the future.

Acknowledgement

Jianwei Guo expresses her thanks to the support of China Scholarship Council.

Appendix A. Supplementary material

Supplementary material related to this article can be found online at http://dx.doi.org/10.1016/j.jcp.2015.10.050.

Appendix B. Closure problems for the velocity

Pb $\mathrm{III}_{(\mathbf{A},m)}$ (in Ω_i):

$$-\mu\triangle\mathbf{A} + \nabla m = 0 \qquad \text{in } \Omega_i \tag{82}$$

$$\nabla\cdot\mathbf{A} = 0 \qquad \text{in } \Omega_i \tag{83}$$

$$\mathbf{n}\cdot(-m\mathbf{I}+\mu(\nabla\mathbf{A}+\nabla\mathbf{A}^T))=\mathbf{0} \quad \text{at } \Sigma_{0,i} \text{ and } \Sigma_{l,i} \tag{84}$$

$$\mathbf{A}(x+l_i)=\mathbf{A}(x) \quad \text{at } \Sigma_{l,i} \tag{85}$$

$$m(x+l_i)=m(x) \quad \text{at } \Sigma_{l,i} \tag{86}$$

$$\mathbf{A}+\mathbf{e}_1=0 \quad \text{at } \Sigma \tag{87}$$

Pb $\mathrm{III}_{(\mathbf{B},s)}$ (in Ω_i):

$$-\mu\triangle\mathbf{B}+\nabla s=0 \quad \text{in } \Omega_i \tag{88}$$

$$\nabla\cdot\mathbf{B}=0 \quad \text{in } \Omega_i \tag{89}$$

$$\mathbf{n}\cdot(-s\mathbf{I}+\mu(\nabla\mathbf{B}+\nabla\mathbf{B}^T))=\mathbf{0} \quad \text{at } \Sigma_{0,i} \text{ and } \Sigma_{l,i} \tag{90}$$

$$\mathbf{B}(x+l_i)=\mathbf{B}(x) \quad \text{at } \Sigma_{l,i} \tag{91}$$

$$s(x+l_i)=s(x) \quad \text{at } \Sigma_{l,i} \tag{92}$$

$$\mathbf{B}+y\mathbf{e}_1=0 \quad \text{at } \Sigma \tag{93}$$

Appendix C. Closure problems for the concentration

Pb III_a (in Ω_i):

$$\mathbf{u}_i\cdot\nabla a=\nabla\cdot(D\nabla a) \quad \text{in } \Omega_i \tag{94}$$

$$a(x+l_i)=a(x) \quad \text{at } \Sigma_{l,i} \tag{95}$$

$$a=0 \quad \text{at } \Sigma_{0,i} \tag{96}$$

$$-\mathbf{n}\cdot D\nabla a=0 \quad \text{at } \Sigma_{\beta\sigma} \text{ and } \Sigma_{l,i} \tag{97}$$

$$\text{(B.C. I)} \quad 1+a=0 \quad \text{at } \Sigma_{\beta\gamma} \tag{98}$$

$$\text{or (B.C. II)} \quad -\mathbf{n}_{ls}\cdot D\nabla a=k(1+a) \quad \text{at } \Sigma_{\beta\gamma} \tag{99}$$

Pb III_b (in Ω_i):

$$v+\mathbf{u}_i\cdot\nabla b=\nabla\cdot(D\nabla b) \quad \text{in } \Omega_i \tag{100}$$

$$b(x+l_i)=b(x) \quad \text{at } \Sigma_{l,i} \tag{101}$$

$$b=0 \quad \text{at } \Sigma_{0,i} \tag{102}$$

$$-\mathbf{n}_{ls}\cdot(\mathbf{e}_2-\nabla b)=0 \quad \text{at } \Sigma_{\beta\sigma} \tag{103}$$

$$\text{(B.C. I)} \quad y+b=0 \quad \text{at } \Sigma_{\beta\gamma} \tag{104}$$

$$\text{or (B.C. II)} \quad -\mathbf{n}_{ls}\cdot D(\mathbf{e}_2+\nabla b)=k(b+y) \quad \text{at } \Sigma_{\beta\gamma} \tag{105}$$

with the momentum equations illustrated by Eqs. (24), (29) and (31) for the above two sets of closure problems.

References

[1] Y. Achdou, O. Pironneau, F. Valentin, Effective boundary conditions for laminar flows over periodic rough boundaries, J. Comput. Phys. 147 (1) (1998) 187–218.
[2] Y. Achdou, C. Sabot, N. Tchou, Transparent boundary conditions for the Helmholtz equation in some ramified domains with a fractal boundary, J. Comput. Phys. 220 (2) (2007) 712–739.
[3] Y. Achdou, P. Le Tallec, F. Valentin, O. Pironneau, Constructing wall laws with domain decomposition or asymptotic expansion techniques, Comput. Methods Appl. Mech. Eng. 151 (1–2) (1998) 215–232.
[4] Y. Achdou, N. Tchou, Boundary value problems with nonhomogeneous Neumann conditions on a fractal boundary, C. R. Math. 342 (8) (2006) 611–616.
[5] R. Avissar, R.A. Pielke, A parameterization of heterogeneous land surfaces for atmospheric numerical models and its impact on regional meteorology, Mon. Weather Rev. 117 (October 1989) 2113–2136.
[6] G.S. Beavers, D.D. Joseph, Boundary conditions at a naturally permeable wall, J. Fluid Mech. (1967) 197–207.
[7] Paul N. Blumberg, Rane L. Curl, Experimental and theoretical studies of dissolution roughness, J. Fluid Mech. 65 (4) (1974) 735–751.
[8] A. Carrau, Moélisation numérique d'un écoulement sur paroi rugueuse, PhD thesis, 1992.
[9] M. Chandesris, D. Jamet, Boundary conditions at a planar fluid–porous interface for a Poiseuille flow, Int. J. Heat Mass Transf. 49 (13–14) (2006) 2137–2150.
[10] G. Dagan, The generalization of Darcy's law for nonuniform flows, Water Resour. Res. 15 (1) (1979) 1–7.
[11] L. Eisenlohr, K. Meteva, F. Gabrovšek, W. Dreybrodt, The inhibiting action of intrinsic impurities in natural calcium carbonate minerals to their dissolution kinetics in aqueous H_2O–CO_2 solutions, Geochim. Cosmochim. Acta 63 (7–8) (1999) 989–1001.
[12] F. Gabrovšek, W. Dreybrodt, A model of the early evolution of karst aquifers in limestone in the dimensions of length and depth, J. Hydrol. 240 (3–4) (2001) 206–224.
[13] B. Goyeau, D. Lhuillier, D. Gobin, M.G. Velarde, Momentum transport at a fluid–porous interface, Int. J. Heat Mass Transf. 46 (21) (2003) 4071–4081.

[14] J. Guo, M. Quintard, F. Laouafa, Dispersion in porous media with heterogeneous nonlinear reactions, Transp. Porous Media (2015), http://dx.doi.org/10.1007/s11242-015-0535-4.
[15] C. Introïni, M. Quintard, F. Duval, Effective surface modeling for momentum and heat transfer over rough surfaces: application to a natural convection problem, Int. J. Heat Mass Transf. 54 (15–16) (2011) 3622–3641.
[16] A.A. Jeschke, K. Vosbeck, W. Dreybrodt, Surface controlled dissolution rates of gypsum in aqueous solutions exhibit nonlinear dissolution kinetics, Geochim. Cosmochim. Acta 65 (1) (2001) 27–34.
[17] W. Jäger, A. Mikelic, N. Neuss, Asymptotic analysis of the laminar viscous flow over a porous bed, SIAM J. Sci. Comput. 22 (6) (2001) 2006–2028.
[18] W. Jäger, A. Mikelić, On the boundary conditions at the contact interface between a porous medium and a free fluid, Ann. Sc. Norm. Super. Pisa, Cl. Sci. 23 (1996) 403–465.
[19] W. Jäger, A. Mikelić, On the roughness-induced effective boundary conditions for an incompressible viscous flow, J. Differ. Equ. 170 (1) (2001) 96–122.
[20] W. Jäger, A. Mikelić, Modeling effective interface laws for transport phenomena between an unconfined fluid and a porous medium using homogenization, Transp. Porous Media 78 (2009) 489–508.
[21] K. Kumar, T. van Noorden, I.S. Pop, Upscaling of reactive flows in domains with moving oscillating boundaries, Discrete Contin. Dyn. Syst., Ser. S 7 (1) (2014) 95–111.
[22] A.C. Lasaga, Kinetic Theory in the Earth Sciences, Princeton University Press, 1998.
[23] H. Luo, M. Quintard, G. Debenest, F. Laouafa, Properties of a diffuse interface model based on a porous medium theory for solid–liquid dissolution problems, Comput. Geosci. 16 (2012) 913–932.
[24] J.A. Ochoa-Tapia, S. Whitaker, Momentum transfer at the boundary between a porous medium and a homogeneous fluid—I. Theoretical development, Int. J. Heat Mass Transf. 38 (14) (1995) 2635–2646.
[25] J.A. Ochoa-Tapia, S. Whitaker, Momentum transfer at the boundary between a porous medium and a homogeneous fluid—II. Comparison with experiment, Int. J. Heat Mass Transf. 38 (14) (1995) 2647–2655.
[26] P.G. Saffman, On the boundary condition at the interface of a porous medium, Stud. Appl. Math. 1 (1971) 93–101.
[27] M. Suzuki, S. Maeda, On the mechanism of drying of granular bed—mass transfer from discontinuous source, J. Chem. Eng. Jpn. 1 (1) (1968) 26–31.
[28] U. Svensson, W. Dreybrodt, Dissolution kinetics of natural calcite minerals in CO_2-water systems approaching calcite equilibrium, Chem. Geol. 100 (1–2) (1992) 129–145.
[29] F.J. Valdés-Parada, J.A. Ochoa-Tapia, J. Alvarez-Ramirez, Diffusive mass transport in the fluid–porous medium inter-region: closure problem solution for the one-domain approach, Chem. Eng. Sci. 62 (21) (2007) 6054–6068.
[30] S. Veran, Y. Aspa, M. Quintard, Effective boundary conditions for rough reactive walls in laminar boundary layers, Int. J. Heat Mass Transf. 52 (15–16) (2009) 3712–3725.
[31] G.L. Vignoles, Y. Aspa, M. Quintard, Modelling of carbon–carbon composite ablation in rocket nozzles, Compos. Sci. Technol. 70 (9) (2010) 1303–1311.
[32] S. Whitaker, The Method of Volume Averaging, Kluwer Academic Publishers, 1999.
[33] B.D. Wood, M. Quintard, S. Whitaker, Jump conditions at non-uniform boundaries: the catalytic surface, Chem. Eng. Sci. 55 (22) (2000) 5231–5245.